Chapter 4

Mini/micro channels

4.1 Convective heat transfer in mini/micro channels

In order to design optimal compact heat exchangers based on mini/micro channels for carbon dioxide cooling which allow us to improve the performances of transcritical cycles, it is essential to properly characterize the convective heat transfer of carbon dioxide at supercritical pressures.

Turbulent convective heat transfer in ducts at supercritical pressure is encountered in a wide variety of engineering situations. Only some of them involve strong dependence of thermodynamic and transport properties on temperature that occurs near the critical point. In these cases, strong coupling between energy and momentum equation gives rise to unconventional effects, which are conventionally defined as critical phenomena [37].

The high working pressure and the favorable heat transfer properties of carbon dioxide enable us to use extruded flat tubes with circular/elliptical ducts, which have diameters much smaller than usual ducts ($d < 2\ mm$) [64]. Size reduction justifies the conventional name of mini/micro channels. Inside each mini/micro channel, the gas cooling process takes place without phase change, since the working fluid is at a supercritical pressure.

Both theoretical and experimental evidences exist which indicate that the idea of a definite critical point, with unambiguous critical temperature, pressure and volume is probably only an approximation; actually there appears to be a critical region [66]. In this critical region the thermophysical properties have a strong dependence on temperature. For each supercritical pressure, the value of temperature at which the specific heat capacity reaches a peak is called pseudo-critical temperature T_{pc} (see Fig. 2.10). At the pseudo-critical temperature, the thermal conductivity shows a weaker peak too (see Fig. 2.12). When the bulk temperature decreases below the pseudo-critical temperature for the considered supercritical pressure, the fluid instantaneously changes from a gas-like state to a liquid-like state [65]. In particular, both density and dynamic viscosity abruptly increase, in order to match the liquid-like behavior (see Figs. 2.9 and 2.13). As a result of the strong dependence of physical properties on temperature, convective heat transfer at supercritical pressures is generally more complex than in common applications. High specific heat capacity, significant thermal expansion, enhanced buoyancy and wall variations of thermal conductivity can produce important influences on convection [67]. Moreover if the physical properties change with temperature, it becomes necessary to take into account the influence of variable physical properties on the turbulent diffusivity expressions [68].

The previous effects probably justify the great discrepancies among different phenomenological correlations, which have been proposed in recent years. A comprehensive review of heat transfer and pressure drop characteristics can be found in [69]. Initially only a few correlations were specifically developed to calculate the heat transfer coefficients during cooling configurations near the critical point. Krasnoshchekov et al. [70] carried out the first experimental study on heat transfer characteristics during turbulent flow in a horizontal tube with carbon dioxide at supercritical pressure under cooling conditions. Baskov et al. [71] found that their measurements for vertical tube were systematically lower than those calculated using the previous formula. They excluded the effect of buoyancy by comparing the results for ascending and descending tubes and proposed a new improved correlation. Petrov and Popov [72] numerically developed a correlation for configurations where free convection is negligible and found good agreement with experimental data. More recently, Pettersen et al. [73] experimentally found for extruded flat tubes with mini/micro channels and carbon dioxide at supercritical pressure that a usual correlation, originally developed for constant properties, can be suitably applied. Pitla et al. [74] proposed that this conventional correlation can be improved by averaging the results obtained with constant properties evaluated at both wall and bulk temperatures. Finally, Yoon et al. [77] found that all previous studies generally under-predict their measurements and proposed a new phenomenological correlation, which adopts the same functional dependence originally proposed by Krasnoshchekov et al. [70]. This brief review clearly shows a circular nature.

Only Liao and Zhao [75] investigated a single horizontal mini/micro channel with supercritical carbon dioxide and found that size reduction causes a heat transfer impairment, which cannot be predicted by correlations developed for normal-sized ducts. Liao and Zhao [75] measured the variation of Nusselt number Nu_b with the bulk mean temperature for various tube diameters, keeping the Reynolds number Re_b, the Prandtl number Pr_b and the difference between the bulk and wall temperature fixed. The Nusselt number was found to decrease as the tube size became smaller and this means that a heat transfer impairment due to size reduction could exist. Liao and Zhao pointed out that buoyancy effects could be responsible for this phenomenon. Since the density changes considerably with temperature near the critical point, free convection can influence heat transfer in supercritical forced flow too. Theoretical considerations lead to the following criterion for negligible buoyancy effects in horizontal tubes [76]:

$$\frac{Gr}{Re_b^2} = \left(\frac{\rho_w}{\rho_b} - 1\right)\frac{g\ d}{u_b^2} < 1 \times 10^{-3}. \tag{4.1}$$

The Grashof number Gr represents the relative strength of secondary flow induced by the buoyancy force. Considering that the buoyancy parameter Gr/Re_b^2 is proportional to the tube diameter d, for each operative configuration a critical diameter exists and all tubes characterized by smaller diameters are free of buoyancy effects. Liao and Zhao found that, for their experimental tests, this critical diameter is comparable to the diameter, which identifies the conventional class of mini/micro channels. They conclude that the heat transfer impairment could be caused, partially at least, by the fact that the buoyancy effect becomes less important for small tubes. In particular, in the region near the pseudo-critical temperature, the experimental data show wall thermal fluxes much lower than those predicted by the correlation of Petrov and Popov [72]. In spite of the fact that the buoyancy effect was not included in the original correlation of Petrov and Popov, Liao and Zhao suggest that the correlation fails when free convection becomes weak or absent, because it was developed based on data for large-diameter tubes where this effect should be significant.

This explanation is not completely satisfactory. For horizontal tubes, buoyancy causes circumferential variations of heat transfer. When buoyancy effects are relevant, the upper part of the tube is characterized by impaired heat transfer while the lower one by enhanced heat transfer, both because of the flow stratification [67]. The small amount of available data does not allow predicting clearly the net result of the two circumferential parts with regard to total heat transfer. Some evidences exist that buoyancy reduces the total heat transfer in horizontal tubes, though not in a very pronounced manner [68]. Firstly, if tested mini/micro channels are characterized by negligible buoyancy effects, a small increase of heat transfer should be expected comparing with large-diameter tubes, contrary to experimental data. Secondly the correlation of Petrov and Popov does not take into account buoyancy effects. In a preliminary work, Petrov and Popov [78] numerically solved a system of equations which included also buoyancy in order to reproduce the experimental results of Baskov et al. [71]. The numerical calculations confirmed that natural convection only slightly affects heat transfer for the values of parameters considered in this experiment. For this reason, in the original paper, where their correlation was proposed, the buoyancy was dropped from the system of equations and no buoyancy parameter was included in the final interpolation formula [72]. The effect of free convection was considered only in a following paper [79].

According to experimental data, mini/micro channels for the considered conditions reveal a peculiar behavior in comparison with large-diameter tubes, i.e. heat transfer impairment, which has not been completely explained yet. Numerical investigation is a useful tool to test additional effects which could explain heat transfer impairment by overcoming some experimental difficulties. Following the work of Petrov and Popov, the present work[1] aims to numerically investigate the turbulent convective heat transfer in mini/micro channels for carbon dioxide at supercritical pressure. A new approach to take into account the effects of variable physical properties on turbulence is proposed, in order to widen the available numerical tools. Three numerical

---

[1] Part of the contents discussed in this chapter was submitted for publication:

- P. Asinari, "Numerical Prediction of Turbulent Convective Heat Transfer in Mini/Micro Channels for Carbon Dioxide at Supercritical Pressure", submitted to *International Journal of Heat and Mass Transfer* (2004).

models are solved for a set of operating conditions which is wide enough for testing their suitability to explain heat transfer impairment in considered conditions. Finally, a comparison with phenomenological correlations developed for normal-sized ducts is also reported.

4.2 Physical models

4.2.1 Conventional approaches

Since the explanation of Liao and Zhao for heat transfer impairment lies on the fact that buoyancy is negligible for some working conditions of mini/micro channels, in the following only pure forced convective regime will be considered. This means that the limiting condition given by Eq. (4.1) is exactly verified. If the gravitational field is neglected, the problem of turbulent convective heat transfer inside horizontal circular tubes shows no angular dependence.

Because of size reduction, the ratio between surface roughness and characteristic diameter increases. The exact profile of the mini/micro channel inner surface becomes more important at smaller diameters and could affect heat transfer too. Experimental data for aluminum mini/micro channels, with the smallest diameter considered in the following, show only negligible discrepancies (6 %) between measured pressure drops and Blasius's correlation, which was developed for hydraulically smooth regime [73]. It is reasonable to suppose that stainless steel mini/micro channels considered by Liao and Zhao were characterized by lower roughness. This hypothesis is confirmed by the fact that the Liao and Zhao correlation is a modified version of the Dittus-Boelter correlation, which does not take into account roughness [75]. Finally, if a roughness effect exists, the analogy between fluid flow and heat transfer leads us to suppose that it should enhance heat transfer, contrary to experimental data. In the following the mini/micro channel will be considered hydraulically smooth over the entire investigated range of Reynolds numbers.

Turbulent forced convection heat transfer is described by the instantaneous conservation equations of continuity, momentum and energy. When the physical properties rapidly change with temperature, as happens near the critical point, the turbulent regime is characterized by high-frequency fluctuations of physical properties, in addition to the usual fluctuations of velocity components and temperature. Reynolds averaging, i.e. time averaging, of governing equations produces additional unknown quantities, which must be calculated in terms of solving variables. In particular, effects due to density are stronger than those due to diffusivities, such as dynamic viscosity and thermal conductivity [80]. For this reason, Favre averaging, i.e. density-weighted averaging, could appear more suitable because density fluctuations are automatically taken into account by this averaging procedure [69]. Unfortunately the problem is only apparently simplified because, in the final system of equations, the density-averaged quantities appear, which differ from the common time-averaged ones. In particular, the phenomenological coefficients of turbulence closure models come from an empirical fitting of time-averaged measurements and they are inapplicable to reduce turbulent quantities due to Favre averaging. For this reason, more usual time-averaging will be used instead of the density-weighted averaging, essentially because extensive validation data for the second approach are lacking. Before proceeding, it is worth to point out that both the thermophysical properties strongly depending on temperature and the few accurate experimental data of convective heat transfer close to the critical point make the validity of modeling for this application somehow questionable. Anyway it is author's opinion that numerical simulations can provide at least some useful selection criteria for the phenomenological correlations.

On introducing the Reynolds decomposition for velocity $\mathbf{u} = \overline{\mathbf{u}} + \mathbf{u}'$ and density $\rho = \overline{\rho} + \rho'$ into instantaneous conservation equations and time-averaging the results, the governing equations of continuity, momentum and energy are obtained, namely

$$\nabla \cdot [\, \overline{\rho}\ (\overline{\mathbf{u}} + \overline{\mathbf{u}}^*)] = 0, \tag{4.2}$$

$$\nabla \cdot [\, \overline{\rho}\, \overline{\mathbf{u}} \otimes (\overline{\mathbf{u}} + \overline{\mathbf{u}}^*)] = -\nabla p + \nabla \cdot \mathbf{S}, \tag{4.3}$$

$$\nabla \cdot \left[\, \overline{\rho}\, \overline{h_T}\ (\overline{\mathbf{u}} + \overline{\mathbf{u}}^*)\right] = -\nabla \cdot \mathbf{q} + \nabla \cdot (\mathbf{S}\, \overline{\mathbf{u}})\,, \tag{4.4}$$

where $\overline{\mathbf{u}}^* = \overline{\rho' \mathbf{u}'} \,/\, \overline{\rho}$ is the characteristic velocity for density fluctuations, $\mathbf{S} = \mathbf{S}^l + \mathbf{S}^t$ is the effective stress tensor and $\mathbf{q} = \mathbf{q}^l + \mathbf{q}^t$ is the effective thermal flux. Laminar and turbulent components for both effective stress tensor and effective thermal flux are defined as follow

$$\mathbf{S}^l = \mu \left(\nabla\overline{\mathbf{u}} + \nabla\overline{\mathbf{u}}^T\right) - (2/3\, \mu\, \nabla \cdot \overline{\mathbf{u}})\ \mathbf{I}, \tag{4.5}$$

$$\mathbf{S}^t = -\overline{\rho}\ \overline{\mathbf{u}' \otimes \mathbf{u}'} - \overline{\rho' \mathbf{u}'} \otimes \overline{\mathbf{u}} - \overline{\rho' \mathbf{u}' \otimes \mathbf{u}'}, \tag{4.6}$$

$$\mathbf{q}^l = -\lambda\ \nabla\ T, \tag{4.7}$$

$$\mathbf{q}^t = \overline{\rho}\ \overline{h'_T \mathbf{u}'} + \overline{\rho' h'_T}\ \overline{\mathbf{u}} + \overline{\rho' h'_T \mathbf{u}'}. \tag{4.8}$$

The last equation can be easily simplified by considering that

$$\overline{h'_T o'} - \overline{h' o'} = 1/2\ \overline{\mathbf{u}' \cdot \mathbf{u}'\, o'} \ll \overline{h' o'}, \tag{4.9}$$

where o can be indifferently ρ, u or v and u and v are the velocity vector components $\mathbf{u} = [u, v]$. Some of the previous terms due to turbulent fluctuations can be expressed by defining turbulent viscosity and gradient-diffusion (see [81] for details), namely

$$-\overline{\rho}\ \overline{\mathbf{u}' \otimes \mathbf{u}'} = (\mu_t/\mu)\ \mathbf{S}^l, \tag{4.10}$$

$$\overline{\rho}\,\overline{h'\mathbf{u'}} = (\lambda_t/\lambda)\,\mathbf{q}^l. \tag{4.11}$$

A tensor $\mathbf{F}^\mu$ can be introduced to describe the effects due to density fluctuations on the effective stress tensor $\mathbf{S} = (\mathbf{I} + \mu_t/\mu\,\mathbf{F}^\mu)\,\mathbf{S}^l$. In the same way, a tensor $\mathbf{F}^\lambda$ can be introduced to describe the effects due to density fluctuations on the effective thermal flux $\mathbf{q} = \left(\mathbf{I} + \lambda_t/\lambda\,\mathbf{F}^\lambda\right)\mathbf{q}^l$, namely

$$\mathbf{F}^\mu = \mathbf{I} + \left(\overline{\rho'\mathbf{u'}} \otimes \overline{\mathbf{u}} + \overline{\rho'\mathbf{u'} \otimes \mathbf{u'}}\right)\left(\overline{\rho}\,\overline{\mathbf{u'} \otimes \mathbf{u'}}\right)^{-1}, \tag{4.12}$$

$$\mathbf{F}^\lambda = \mathbf{I} + \left(\overline{\rho'h'}\,\overline{\mathbf{u}} + \overline{\rho'h'\mathbf{u'}}\right) \otimes \overline{h'\mathbf{u'}} / \left(\overline{\rho}\,\overline{h'\mathbf{u'}} \cdot \overline{h'\mathbf{u'}}\right). \tag{4.13}$$

In particular, density fluctuations affect both diffusive and convective terms into Eqs. (4.2, 4.3, 4.4). Since $\mathbf{F}^\mu$ is not symmetric, then the effective stress tensor $\mathbf{S}$ is not symmetric either.

Keeping in mind the geometrical configuration realized by mini/micro channels, a two dimensional computational domain $\Omega \in \mathbb{R}^2$ will be considered and a set of cylindrical coordinates will be adopted to describe it, namely $\Omega = \{(x,r) \in \mathbb{R}^2 : \ 0 \leq x \leq L \ , \ 0 \leq r \leq R\}$. The velocity vector components will be accordingly renamed $\overline{\mathbf{u}} = (\overline{u}, \overline{v})$. Even though the problem concerned can have local distortions and variations in the velocity and temperature field, the boundary layer theory [82] can be considered as a preliminary modeling approach in order to reduce the computational demand and to increase the number of simulations needed by statistical regression. Because of these simplifying assumptions, the momentum and energy equation can be simplified to yield the following expressions

$$\nabla_{xr} \cdot [\,\overline{\rho}\ (\overline{\mathbf{u}} + \overline{\mathbf{u}}^*)] = 0, \tag{4.14}$$

$$\nabla_{xr} \cdot [\,\overline{\rho}\,\overline{u}\,(\overline{\mathbf{u}} + \overline{\mathbf{u}}^*)] = -\frac{d\,p}{d\,x} + \frac{1}{r}\frac{\partial}{\partial r}\,(r\ S_{xr})\,, \tag{4.15}$$

$$\nabla_{xr} \cdot \left[\,\overline{\rho}\,\overline{h_T}\ (\overline{\mathbf{u}} + \overline{\mathbf{u}}^*)\right] = +\frac{1}{r}\frac{\partial}{\partial r}\,(r\,\overline{u}\,S_{rx} - r\,q_r)\,. \tag{4.16}$$

Simplifying the laminar stress tensor, then all the components of effective stress tensor can be expressed in terms of the transverse velocity gradient. In the same way, the concept of thermal boundary layer simplifies the calculation of thermal fluxes. Simplifying the laminar thermal flux, then all the components of effective thermal flux can be expressed in terms of transverse temperature gradient. The previous simplifications yield:

$$\mathbf{S}^l \approx \left[\begin{array}{cc} 0 & \mu\,\partial_r \overline{u} \\ \mu\,\partial_r \overline{u} & 0 \end{array} \right], \tag{4.17}$$

$$\mathbf{S} \approx \left[\begin{array}{cc} \mu^t\, F^\mu_{xr}\, \partial_r \overline{u} & (\mu + \mu^t\, F^\mu_{xx})\, \partial_r \overline{u} \\ (\mu + \mu^t\, F^\mu_{rr})\, \partial_r \overline{u} & \mu^t\, F^\mu_{rx}\, \partial_r \overline{u} \end{array} \right], \tag{4.18}$$

$$\mathbf{q}^l \approx \left[\, 0, \lambda\, \partial_r T \,\right]^T, \tag{4.19}$$

$$\mathbf{q} \approx \left[\, \lambda^t\, F^\lambda_{xr}\, \partial_r T, (\lambda + \lambda^t\, F^\lambda_{rr})\, \partial_r T \,\right]^T. \tag{4.20}$$

In the following some components of the tensors, which describe density fluctuations, are reported because they are involved in the calculation of effective diffusive terms S_{xr}, S_{rx} and q_r in simplified Eqs. (4.15, 4.16), namely

$$F^\mu_{xx} = 1 + \frac{\overline{\rho' u'}\ \overline{v}}{\overline{\rho}\ \overline{u'v'}} + \frac{\overline{\rho' u' v'}}{\overline{\rho}\ \overline{u'v'}}, \tag{4.21}$$

$$F^\mu_{rr} = 1 + \frac{\overline{\rho' v'}\ \overline{u}}{\overline{\rho}\ \overline{u'v'}} + \frac{\overline{\rho' u' v'}}{\overline{\rho}\ \overline{u'v'}}, \tag{4.22}$$

$$F^\lambda_{rr} = 1 + \frac{\overline{\rho' h'}\ \overline{v}}{\overline{\rho}\ \overline{h'v'}} + \frac{\overline{\rho' h' v'}}{\overline{\rho}\ \overline{h'v'}}. \tag{4.23}$$

The off-diagonal components of the effective stress tensor may differ, i.e. $S_{xr} \neq S_{rx}$, because in general $F^\mu_{xx} \neq F^\mu_{rr}$. The term F^μ_{xx} directly affects the turbulent viscosity, while the term F^μ_{rr} describes the effect of density fluctuations on viscous heating, which can be usually neglected. For this reason, all considered models assume $F^\mu_{rr} \approx 1$ and consequently $S_{rx} \approx (1 + \mu_t/\mu)\, S^l_{rx} = (1 + \mu_t/\mu)\, S^l_{xr}$.

In order to quantify the importance of the density fluctuations along radial direction, an auxiliary radial velocity $\overline{v}_0$ is introduced, which represents the radial velocity field obtained neglecting density fluctuations. Assuming fixed the mean density distribution, this auxiliary function satisfies the following equation

$$\frac{\partial}{\partial x}\left(\overline{\rho}\,\overline{u}\right)+\frac{1}{r}\frac{\partial}{\partial r}\left(r\,\overline{\rho}\,\overline{v}_0\right)=0. \tag{4.24}$$

Along the axial direction, the effect of density fluctuations can be clearly neglected $|\overline{u}^*| \ll |\overline{u}|$. Along radial direction, considering Eqs. (4.14, 4.24) and applying proper boundary conditions, a relation among actual, characteristic and auxiliary radial velocities can be found $\overline{v}+\overline{v}^* = \overline{v}_0$. In the region near the critical point, strong density fluctuations ensure $|\overline{v}^*| \gg |\overline{v}_0|$. For all the following calculations, this condition has been verified for at least one order of magnitude. In this case, an easier correlation yields $\overline{v}+\overline{v}^* \approx 0$ and it can be applied to simplify Eqs. (4.21, 4.23).

Finally, density fluctuations must be related to velocity fluctuations involved into turbulence closure models. The key idea is to expand the equation of state $\rho(h,\,p)$ by considering fluctuations of independent variables $\rho' = \partial_h\overline{\rho}|_p\,h' + \partial_p\overline{\rho}|_h\,p'$. Neglecting pressure variations, the residual term can be expressed by means of a modified compressibility $\beta = -\partial_h\overline{\rho}|_p/\overline{\rho}$, in order to find the final correlation $\rho' = -\overline{\rho}\;\beta\;h'$. This correlation can be applied into the definition of characteristic velocity due to density fluctuations $\overline{\mathbf{u}}^* = -\beta\;\overline{h'\mathbf{u}'}$, which influences the convective terms, and into the definitions of correction factors F^{μ}_{xx} and F^{λ}_{rr}, which influence the diffusive terms, and are defined as

$$F^{\mu}_{xx} = 1-\beta^2\,\frac{\overline{h'u'}\;\overline{h'v'}}{\overline{u'v'}}-\beta\,\frac{\overline{h'u'v'}}{\overline{u'v'}}, \tag{4.25}$$

$$F^{\lambda}_{rr} = 1-\beta^2\,\overline{h'h'}\;-\beta\,\frac{\overline{h'h'v'}}{\overline{h'v'}}. \tag{4.26}$$

For calculating effective diffusivities, a turbulence closure model is needed. How physical properties varying with temperature influence the turbulent diffusivity expressions has not been systematically investigated [68]. Therefore, many different assumptions have been proposed for models based on the mixing length concept, which were originally developed for fluids with constant properties [82]. Semi-empirical correlations exist which express turbulent diffusivities as functions of a dimensionless distance from the wall $y^+ = (R - r)\sqrt{\overline{\rho}_x\,\tau_w}/\mu_x$, which can be useful to characterize the fluid-wall interaction [82]. Some authors assumed that the original correlations may be used without changes, if proper values of physical properties are considered to compute dimensionless distance y^+. Deissler [83] proposed using the wall properties ($\overline{\rho}_x = \overline{\rho}_w$ and $\mu_x = \mu_w$), Sastry [84] the local properties ($\overline{\rho}_x = \overline{\rho}$ and $\mu_x = \mu$) and Goldmann [85] proposed an integral formulation between previous extremes, based on a theoretical hypothesis on local turbulence characteristics, namely

$$y^+ = \int_{R-r}^{R} \frac{\sqrt{\overline{\rho}\,\tau_w}}{\mu}\,dr. \tag{4.27}$$

The method proposed by Goldmann produces better agreement with experimental heat transfer data [68].

The discussed features are shared by all considered models. Essentially they differ for the way of computing the usual turbulent diffusivities with variable thermophysical properties and the corrective factors due to density fluctuations. Three physical models will be considered: the model of Petrov and Popov [72, 78], the model of Bellmore and Reid [86] and finally the proposed model.

Petrov and Popov applied the mixing length model to calculate the turbulent diffusivities. They adopted Sastry's approach to take into account variable thermophysical properties but considered an additional corrective procedure to compute effective values, based on the discrepancies between shear stresses computed with constant and variable properties. They totally neglected the effects due to density fluctuations and so implicitly assumed $F^{\mu}_{xx} = F^{\lambda}_{rr} = 1$.

Bellmore and Reid applied the mixing length model too and adopted the Goldmann approach to take into account variable thermophysical properties. They proposed an innovative method to include density fluctuations in the equations of turbulent transport. The main topics of mixing length theory will be summarized in order to understand the approach due to Bellmore and Reid. In the following expressions, a new formal convention for time averaging will be temporarily considered $\langle o \rangle \equiv \overline{o}$. The mixing length theory is based on two heuristic assumptions [82]

$$\langle u'v' \rangle = +C_{uv} \, \langle |u'| \rangle \langle |v'| \rangle, \tag{4.28}$$

$$\langle h'v' \rangle = -\zeta \, C_{hv} \, \langle |h'| \rangle \langle |v'| \rangle, \tag{4.29}$$

where $\zeta = \partial_r \, \overline{h} / |\partial_r \, \overline{h}|$, $0 < C_{uv} < 1$ and $0 < C_{hv} < 1$. The signs in both expressions are due to experimental evidence. In particular the sign in Eq. (4.28) depends on the fact that v is the velocity component aligned along the radial direction pointing towards the wall. If the average absolute deviations $\langle |x| \rangle$ were replaced by the standard deviations $\langle x^2 \rangle^{1/2}$ in the heuristic assumptions, the correlation coefficients would appear. If the velocity fluctuations are normally distributed, there is a definite relationship between the average absolute deviation and the standard deviation [87]. Unfortunately almost every turbulent flow occurring in practice is characterized by inhomogeneous turbulence [81]. For this reason, robust statistics, i.e. average absolute deviation, is preferable and the Eqs. (4.28, 4.29) will be considered as the definitions of robust correlation coefficients. Each average absolute deviation can be expressed by transverse velocity gradient or transverse enthalpy gradient: this means $\langle |u'| \rangle = l_u \, |\partial_r \, \overline{u}|$, $\langle |v'| \rangle = l_v \, |\partial_r \, \overline{u}|$ and $\langle |h'| \rangle = l_h \, |\partial_r \, \overline{h}|$. Introducing these expressions into the previous assumptions given by Eqs. (4.28, 4.29) and grouping the unknown terms, two essential quantities emerge: the mixing length $l_m = (C_{uv} \, l_u \, l_v)^{1/2}$ and the turbulent Prandlt number $Pr_t = C_{uv} \, l_u / (C_{hv} \, l_h)$, namely

$$\langle u'v' \rangle = l_m^2 \, |\partial_r \, \overline{u}|^2, \tag{4.30}$$

$$\langle h'v'\rangle \; = \; -\zeta\,(l_m^2/Pr_t)\,|\partial_r\,\overline{h}|\,|\partial_r\,\overline{u}|. \tag{4.31}$$

Both quantities are supplied by turbulence closure models, based on the mixing length concept. Bellmore and Reid essentially interpreted the definitions of correlation coefficients due to robust statistics in a factorized form and this yields

$$\langle u'v'\rangle \; = \Delta u\;\Delta v, \tag{4.32}$$

$$\langle h'v'\rangle \; = \Delta h\;\Delta v, \tag{4.33}$$

where $\Delta u = b_1\,\langle|u'|\rangle$, $\Delta v = b_2\,\langle|v'|\rangle$ and $\Delta h = -\zeta\;b_3\,\langle|h'|\rangle$. The congruence with the original heuristic assumptions implies that $b_1\,b_2 = C_{uv}$ and $b_2\,b_3 = C_{hv}$ but these constraints are not sufficient to unambiguously determine the constants b_i. Equation (4.30) suggests that the velocity fluctuations along both directions produce comparable effects. The condition $\Delta u = \Delta v$ allows us to produce an additional constraint $b_1\,l_u = b_2\,l_v$. In this way, the values of the constants are found, namely $b_1 = (C_{uv}\,l_v/l_u)^{1/2}$, $b_2 = (C_{uv}\,l_u/l_v)^{1/2}$ and $b_3 = C_{hv}\,C_{uv}^{-1/2}\,(l_v/l_u)^{1/2}$. The main advantage of the recasted Eqs. (4.32, 4.33) is that each function Δo depends only on the fluctuations of the same variable o' and it can be calculated by means of the mixing length theory. In analogy with this factorization, Bellmore and Reid proposed the following general decomposition

$$\langle (u')^{n_1}(v')^{n_2}(h')^{n_3}\rangle \; = \; (\Delta u)^{n_1}\,(\Delta v)^{n_2}\,(\Delta h)^{n_3}\,, \tag{4.34}$$

where $n_i \in \mathbb{N}^+$. For example, considering $n_1 = n_3 = 1$ and $n_2 = 0$, the expression for turbulent thermal diffusivity along axial direction can be found, namely

$$\langle h'u'\rangle \; = \; \Delta h\;\Delta u = -\zeta\;(C_{hv}\,l_v/l_u)\,\langle|h'|\rangle\langle|u'|\rangle = -\zeta\;C_{hu}\,\langle|h'|\rangle\langle|u'|\rangle. \tag{4.35}$$

Similarly we can proceed with all turbulent terms involved into Eqs. (4.25, 4.26), which can be calculated by means of the general decomposition given by Eq. (4.34).

Recalling Eqs. (4.33, 4.35), the characteristic velocity due to density fluctuations can be expressed as

$$F_{xx}^{\mu} = F_{rr}^{\lambda} = \phi_{BR} = 1 + \zeta\, \beta\, \sigma_{BR} - \beta^2\, \sigma_{BR}^2, \tag{4.36}$$

$$\overline{u}_{BR}^{*} = \overline{v}_{BR}^{*} = \zeta\, \beta\, \left(l_m^2\, |\partial_r \overline{u}| / Pr_t \right)\, |\partial_r \overline{h}|, \tag{4.37}$$

where $\sigma_{BR} = (l_m/Pr_t)\, |\partial_r \overline{h}|$ can be considered an index of intensity for density fluctuations. We can now discuss the effects due to density fluctuations. Since $\beta\, \sigma_{BR}$ is usually a small quantity also near the critical point, we can suppose $\phi_{BR} \approx 1 + \zeta\, \beta\, \sigma_{BR}$. This means that during cooling conditions ($\zeta < 0$), density fluctuations reduce turbulent diffusivities ($\phi_{BR} < 1$), while during heating conditions ($\zeta > 0$) they substantially increase turbulent diffusivities ($\phi_{BR} > 1$). Additional convective terms along the axial direction are negligible. The radial velocity field in absence of density fluctuations $\overline{v}_0$ can be discussed by Eq. (4.24). Let us define a vectorial velocity in the absence of density fluctuations $\overline{\mathbf{u}}_0 = (\overline{u}, \overline{v}_0)$. For mini/micro channels, the density gradient can be reasonably assumed orthogonal to this velocity $\overline{\mathbf{u}}_0 \cdot \nabla \rho \approx 0$, because $\overline{\mathbf{u}}_0$ is approximately oriented along streamlines. In this way, Eq. (4.24) easily yields that $-\zeta\, \overline{v}_0 \geq 0$. Recalling that $\overline{v} \approx -\overline{v}^*$ and $\zeta\, \overline{v}^* \propto (\partial_r \overline{h})^2 \geq 0$ by definition, a similar correlation for the effective radial velocity is found $-\zeta\, \overline{v} \geq 0$. Since $|\overline{v}| \gg |\overline{v}_0|$, then density fluctuations increase convective radial terms both during cooling conditions ($\overline{v} \gg \overline{v}_0 \geq 0$) and heating conditions ($\overline{v} \ll \overline{v}_0 \leq 0$).

4.2.2 Proposed turbulence closure model

Both previous models are unsatisfactory for some reasons. The distinguishing features will be organized into three different categories: the turbulence closure model for common terms due to time averaging, the procedure to take into account variable physical properties and, finally, the turbulence closure model for additional terms due to density fluctuations.

Both previous models use turbulent models based on the mixing length concept. Although some generalizations were proposed, these models have some drawbacks [81]. Firstly, they strongly depend on the geometry of the considered flow to formulate practical relations for the mixing length, hence they are not general. Secondly, they prescribe that turbulent diffusivities be zero where there is no velocity gradient, as it happens for the centerline of mini/micro channels, although this clashes with the experimental evidence [81]. Concerning variable physical properties, the previous models differ for the considered operative procedure, but they substantially adopt common correlations by reducing the problem to calculate a modified y^+. In particular, they do not modify the functional nature of the correlations. Instead variable properties probably modify the local turbulent phenomena, which only a model based on differential equations can describe. Finally, only the model of Bellmore and Reid considers the density fluctuations. This model is based on the possibility to calculate average absolute deviations by means of the mixing length concept. This possibility is not accessible by most widespread turbulence models and it would require to know statistical distribution for each variable. As a result, the discussed method is only valid for the simplest turbulence model and it is not directly generalizable. Moreover, Eq. (4.35), which has been deduced according to the generalized decomposition given by Eq. (4.34), is in contrast with the gradient-diffusion hypothesis because it depends on the radial enthalpy gradient instead of the axial one as expected because it involves the axial velocity component.

A different approach is proposed. Before proceeding to describe the constitutive hypotheses, some explanations on the mathematical meaning of the general decomposition proposed by Bellmore and Reid given by Eq. (4.34) are required. Within the framework of the mixing length theory, the turbulence closure model can be considered a tool which allows us to calculate robust correlation coefficients $C_{uv} = l_m^2/(l_u\, l_v)$ and $C_{hv} = l_m^2/(Pr_t\, l_v^2)$. Analogously, when Eq. (4.35) is considered, the general decomposition reduces to suppose $C_{hu} = C_{hv}\, l_v/l_u$. The coefficients b_i involved in factorized heuristic assumptions given by Eqs. (4.32, 4.33) can be expressed as functions of second-order mixed robust correlation coefficients C_{hv}, C_{hu} and C_{uv}, which are the non-zero lowest-order coefficients. Substituting these expressions into Eq. (4.34), a modified expression is found

$$\langle (u')^{n_1} (v')^{n_2} (h')^{n_3} \rangle \;=\; (-\zeta)^{n_3}\;\, C_{hv}^{q_1}\, C_{hu}^{q_2}\, C_{uv}^{q_3}\; \langle |u'| \rangle^{n_1} \langle |v'| \rangle^{n_2} \langle |h'| \rangle^{n_3}, \tag{4.38}$$

where $q_i \in \mathbb{Q}$ is defined as $q_i = \sum_{j=1}^{3} (1 - 2\, \delta_{ij})\, n_j/2$ and δ_{ij} is the Kronecker's operator. Mathematically, the general decomposition given by Eq. (4.34) is equivalent to suppose that higher-order robust correlation coefficients are proper combinations of lower-order ones. Since, by definition $n_i = \sum_{j=1}^{3} (1 - \delta_{ij})\, q_j$ and recalling the expressions for lower-order correlation coefficients given by Eqs. (4.32, 4.33, 4.35), the previous decomposition can be modified as

$$\langle (u')^{n_1} (v')^{n_2} (h')^{n_3} \rangle \;=\; (-\zeta)^{n_3}\;\, |\langle h' v' \rangle|^{q_1}\, |\langle h' u' \rangle|^{q_2}\, \langle u' v' \rangle^{q_3}. \tag{4.39}$$

This correlation has been rigorously demonstrated within the framework of the theory developed by Bellmore and Reid and so it can be considered equivalent to the decomposition given by Eq. (4.34). The main advantage is that it involves only quantities that are calculated by all turbulence closure models because they emerge from time averaging of flow equations with constant properties. Essentially the previous relation assumes a general dependency of terms due to density fluctuations from usual terms due to velocity fluctuations. It can be considered as a constitutive hypothesis without any dependence on a particular turbulence model. In the following, the turbulent viscosity hypothesis given by Eq. (4.10) and the gradient-diffusion hypothesis given by

Eq. (4.11) will be considered in order to produce a meaningful example without loss of generality. Applying Eq. (4.39) to all turbulent terms involved into Eqs. (4.25, 4.26), we find again the same formal expression for the corrective factor ϕ which influences effective diffusivities given by Eq. (4.36), but with a different intensity index σ, given by

$$\sigma = \sqrt{\frac{\lambda_t^2}{\overline{\rho}\,\mu_t}\,\frac{|\partial_x T\,\partial_r T|}{|\partial_r \overline{u}|}}. \tag{4.40}$$

We can proceed in the same way for the characteristic velocity, obtaining

$$\overline{u}^* = \zeta\;\beta\;(\lambda_t/\overline{\rho})\;|\partial_x T| \ll \overline{v}^* = \zeta\;\beta\;(\lambda_t/\overline{\rho})\;|\partial_r T|. \tag{4.41}$$

Since these relations involve the temperature gradient, contrarily to previous ones which involve enthalpy gradient, the effects due to compressibility must be discussed. For both axial and radial direction, the generic component of the enthalpy gradient can be expressed by means of temperature and pressure changes $\partial_i \overline{h} = c_p\,T\,[\,\partial_i T/T - \varphi\,\partial_i\,p/p\,]$, where c_p is the specific heat capacity $c_p = \partial_T \overline{h}|_p$ and the dimensionless parameter φ takes into account non-ideal gas effects

$$\varphi = \frac{\beta\,c_p\,T - 1}{\overline{\rho}\,c_p\,T/p}. \tag{4.42}$$

In all the following calculations, this parameter is included over the range $0 < \varphi < 0.21$. Since the relative temperature changes are much greater than relative pressure changes $\partial_i T/T \gg \partial_i\,p/p$, then the compressibility effects on enthalpy can be neglected and an approximate relation yields $\partial_i \overline{h} \approx c_p\,\partial_i T$. According to the boundary layer theory, this approximation is even more satisfied along the radial direction. For comparing the previous results with those obtained by Bellmore and Reid, Eqs. (4.36, 4.37) will be directly generalized by expressing mixing length and turbulent Prandtl number as functions of turbulent diffusivities. Recalling that $l_m = \mu_t^{1/2}\,(\rho\,|\partial_r \overline{u}|)^{-1/2}$ and $Pr_t = \mu_t\,|\partial_r \overline{h}|\,(\lambda_t\,|\partial_r T|)^{-1}$, the generalized expressions for the intensity index and for the components of characteristic velocity become

$$\sigma_{BR} = \sqrt{\frac{\lambda_t^2}{\overline{\rho}\,\mu_t}\,\frac{|\partial_r T|^2}{|\partial_r \overline{u}|}}, \tag{4.43}$$

$$\overline{u}^*_{BR} = \overline{v}^*_{BR} = \zeta\ \beta\ (\lambda_t/\overline{\rho})\ |\partial_r T|. \tag{4.44}$$

Despite the simplicity of the procedure, Eqs. (4.43, 4.44) can be calculated by any turbulence model too. In this second case, the intensity index σ_{BR} depends only on radial temperature gradient, while the intensity index σ calculated by the proposed approach depends on the temperature gradient along both directions. If density fluctuations are due to enthalpy fluctuations and the latter ones satisfy the gradient-diffusion hypothesis by given Eq. (4.11), which is strongly anisotropic, it is not clear why the effects due to density fluctuations should be isotropic. Since the original formulation of Bellmore and Reid was developed for boundary layer flow, the generalized Eqs. (4.43, 4.44) overestimate the effect of axial density fluctuations and they are not universally valid. Here an essential feature of the proposed model emerges. Equations (4.40, 4.41) involve the axial gradient to predict the effects due to density fluctuations along the axial direction. This feature essentially predicts a lower effect of density fluctuations on turbulent diffusivities since $\sigma \ll \sigma_{BR}$, because usually $|\partial_x T| \ll |\partial_r T|$. Concerning the effects on convective terms, the two formulations are formally equivalent for the radial direction $\overline{v}^* = \overline{v}^*_{BR}$, while they again differ for the axial direction $\overline{u}^* \ll \overline{u}^*_{BR}$. Since the latter effect is negligible in the considered application, the essential difference between the two approaches for simulation of mini/micro channels lies in the description of the effective diffusivities and, in particular, in the fact that $|\phi - 1| \ll |\phi_{BR} - 1|$.

Any turbulence closure model can be applied to calculate turbulent diffusivities into Eqs. (4.40, 4.41). As discussed previously, it is recommended to adopt models based on differential equations. They can easily take into account effects due to variable physical properties because they need no particular correlations, as those involved in the mixing length model developed for constant-property flows [81]. Additional differential equations increase the computational effort but there is no need to include additional terms due to fluctuating properties within these equations, since they are directly formulated for time-averaged quantities. In the following, two 2-equation models will be considered in order to compare the effects due to the description of turbulent diffusivities. The standard $k-\epsilon$ model [88] is considered because of its popularity in many engineering fields. It is based on the solution of two separate transport equations which allow us to compute turbulence kinetic energy (k) and its dissipation rate (ϵ) in order to estimate turbulent diffusivities [89]. The other considered model is the RNG $k-\epsilon$ model [90] which can be partially developed by means of the renormalization group theory. Briefly, in some applications the RNG $k-\epsilon$ model improves the accuracy for near-wall flows, by considering more accurate transport equations and a variable ratio between turbulent viscosity and turbulent thermal conductivity, contrarily to the previous model. The original formulation included the possibility to use a 2-equation approach very close to the wall too, i.e. at low Reynolds numbers. In the discussed simulations, this possibility will not be used. In this way, the two models are based on the same number of equations in all calculation sub-domains. Since both 2-equation models were formulated for fully-developed turbulence, they are not usually applied in the near-wall region [89]. In the region where the effect of molecular viscosity cannot be neglected (approximately $0 < y^+ < 60$), an additional resolution technique must be supplied. Usually, a smaller number of equations is used in this region. Semi-empirical algebraic correlations, which involve no differential equation, were developed for flows with constant properties and they are conventionally called wall functions. As previously discussed for mixing length correlations, variable physical properties may compromise the suitability of wall functions [91]. The minimum successful strategy, i.e. 1-equation model, will be adopted in the near-wall region. The whole calculation domain is subdivided into a viscosity-affected region, which is a little wider than the laminar viscous sublayer, in order to include the transition layer, and a fully-turbulent region [81]. In the latter, the standard $k-\epsilon$ and the RNG $k-\epsilon$ models can be applied, while in the viscosity-affected region the turbulent diffusivities are assumed as exclusive functions of turbulence kinetic energy [92,93]. A proper blending function [94] between the previous calculation procedures completes the method, which is usually referred to as two layer zonal model.

A proper set of boundary conditions is needed to solve the system of equations. At the inlet boundary, some unknown quantities, which describe the fluid flow, are supposed uniformly distributed along the radial direction: $\overline{u}(0,r) = u_0$, $\overline{v}(0,r) = 0$ and $T(0,r) = T_0$. We can proceed in same way for turbulent quantities involved into 2-equation models, i.e. the turbulence kinetic energy $k(0,r) = k_0$ and the turbulence dissipation rate $\epsilon(0,r) = \epsilon_0$. Usual relations are used to calculate turbulence quantities by means of more convenient quantities involved into fluid flow, such as the average Reynolds number and the mean axial velocity [89]. At the outlet boundary, the only calculation unknown which was not considered within inlet conditions, i.e. pressure, is imposed $p(L) = p_L$. Since the solution is necessarily axisymmetric, no radial gradient is allowed for any solved quantity at the centerline of the mini/micro channel. At the wall boundary a given thermal flux $\partial_r T = q_w/\lambda$ or, alternatively, a given wall temperature $T(x,R) = T_w$ is considered. Velocity components are specified according to no-slip boundary conditions: $\overline{u}(x,R) = 0$ and $\overline{v}(x,R) = 0$. At the wall boundary the turbulent quantities are $k(x,R) = 0$ and $\epsilon(x,R) = \epsilon_w$, where ϵ_w can be calculated by means of a simplified approximation for the turbulent length-scale at the wall [92]. The previous set of physical conditions is insufficient to determine a well-posed mathematical problem: additional information is produced by linear extrapolation of the interior computational domain. This strategy yields a more stable resolution process than that based on the splitting between physical quantities at the inlet and extrapolated quantities at the outlet. Since the pressure gradients along short mini/micro channels are negligible, this strategy will not reduce the physical accuracy.

For fluids at supercritical pressure near the critical point, the precise measurement of physical properties is not easily attainable. Technical improvement probably justifies some discrepancies among physical property databases, developed during the last years. These inaccuracies could obviously affect the numerical simulations. In particular, the correlation of Petrov and Popov was derived by interpolating some numerical tests, which adopted a merged database based on two different sets of experimental data [72]. They tried to overcome the lack of accuracy for thermal conductivity near the pseudo-critical temperature, which characterized the experimental results of Altunin [95]. In the following calculations, a recently developed database for thermophysical properties of carbon dioxide is considered [96]. For this database, the estimated uncertainty ranges are $0.15 - 1.5\,\%$ for specific heat capacity, less than $5\,\%$ for thermal conductivity, $0.03 - 0.05\,\%$ for density and finally $0.3 - 5\,\%$ for viscosity. In the previous ranges, the highest values refer to liquid-like states or the highest pressures, because these conditions realize configurations which are more difficult to be accurately measured.

4.3 Numerical discretization and solution procedure

The governing equations of continuity (4.14), momentum (4.15) and energy (4.16) conservation were discretized, according to the finite volume method [97]. Essentially the solution domain was subdivided into a finite number of small control volumes. There was a significant benefit to be obtained by arranging unknowns for velocity components on a different grid from that used for all other variables. This strategy, called staggered grid, was adopted [53]. This means that unknown velocity components were located at the control volumes faces, which surrounded the computational nodes for residual variables. Since there were two different computational grids, some interpolations were needed to complete missing information. In particular, to solve the momentum Eq. (4.15), the face-centered values for pressure were interpolated using momentum equation coefficients and this allowed us to estimate the effective viscosity at the volume-centered node [89]. Some interpolations were needed for convective terms too. In this case, the convective term in the momentum equation is non-linear and this seems to make the resolution process more complicate. Since the final solution process will be essentially iterative, the non-linear terms were approximated at each iteration. The outer iteration was used to estimate the non-linear coefficients. This essentially linearized the momentum equation and made it similar to other equations [97]. The general upwind scheme was adopted to calculate the convective terms for all linearized equations [53]. It sets the face-centered values for all variables equal to the volume-centered values in the upstream volumes. The identification of upstream volumes was done according to the approximated velocity field. The previously discussed turbulence models, which take into account the effects due to density fluctuations, involve some additional source terms in the governing equations, which were properly discretized.

4.3.1 Discretization of the database for thermophysical properties

For the considered application, both thermophysical database and computational domain must be properly discretized. Since for short mini/micro channels pressure drops are negligible, the thermophysical properties can be considered as functions of temperature only. Physical properties can be grouped into two different sets. The first set, which includes the specific heat capacity, c_p, the thermal conductivity, λ, and the modified compressibility, β, involves thermophysical properties which show a peak near the pseudo-critical temperature for a given range of supercritical pressures. For this reason they are defined non-monotonic properties. The second set, which includes density, ρ, and dynamic viscosity, μ, involves thermophysical properties which decrease monotonically with temperature. The considered database [96] discriminates property changes due to very small temperature differences, which, near the critical temperature, are approximately comparable to 1 mK. The high-resolution capacity of this database produces a great amount of information, which would slow down the upgrade of physical properties during the resolution process. For this reason, piecewise linear approximations will be adopted and the distribution of nodal values will be properly chosen. If the generic property $f(T)$ is considered, the problem reduces to finding the optimal distribution T_i where $1 \leq i \leq N_f$ and the corresponding one $f_i = f(T_i)$ which ensure the desired accuracy. Between two consecutive nodal values T_i and T_{i+1}, the function will be approximated by means of a linear function $\tilde{f}_{i,i+1}(T) = f_i - (f_{i+1} - f_i)\,(T - T_i)/(T_{i+1} - T_i)$ where $T_i < T < T_{i+1}$. A local relative error $\tilde{e}_{i,i+1} = \max\left(|f - \tilde{f}_{i,i+1}|/f\right)$ can be assigned to the same temperature range and a global relative error $e = \max_i(\tilde{e}_{i,i+1})$ can be assigned to the whole temperature range by considering i into the range $1 \leq i \leq N_f - 1$. If the initial temperature T_1 is given, the optimal distribution can be unambiguously defined as the minimum number of nodal values which guarantees that the global relative error is upper-bounded $e_f \leq e_f^0$. The parameter e_f^0 is the error threshold for the considered piecewise linear approximation of the generic property $f(T)$. This parameter determines the smallest temperature difference involved into the whole approximation $\Delta T_m(e_f^0) = \min_i (T_{i+1} - T_i)$ for i into the range $1 \leq i \leq N_f - 1$. By definition, $\Delta T_m(0)$ represents the resolution of the original database. Each piecewise approximation allows us to reduce the number of nodal values by increasing the smallest temperature difference $\Delta T_m(e_f^0) \geq \Delta T_m(0)$. Now this approach will be turned over. The total number of nodal values, N_f, will be considered a fixed constraint for all the physical properties and for all supercritical pressures. This constraint depends on what run time can be considered acceptable in the considered application. In this way, the highest error thresholds will appear for non-monotonic properties and for the lowest supercritical pressure, i.e. where the strongest changes exist. In the following calculations, the error thresholds are $0.3 - 5.6\,\%$ for heat capacity, $0.1 - 2\,\%$ for thermal conductivity, $0.1 - 0.5\,\%$ for modified compressibility and $0.1 - 0.5\,\%$ for both monotonic properties. For density and specific heat capacity, the piecewise linear approximations produce errors greater than the estimated uncertainties for the same quantities. In particular, the error threshold for heat capacity appears quite high. The minimum temperature difference involved into the approximation of heat capacity is considerably greater than that of the original database $\Delta T_m(0.056) = 5\; mK > 1\; mK$, but it is smaller than the temperature differences which the discretized computational domain allows us to estimate.

4.3.2 Local grid refinement

Let us consider the discretization of the computational domain. According to the boundary layer theory, the unknown quantities are characterized by axial gradients which are much smaller than radial ones. For this reason, an axially homogeneous mesh and a characteristic length of the generic control volume Δx comparable to the radial dimension can be adopted. Three different meshes were considered in order to test the dependence of the results on this parameter and they produced approximately the same results. For this reason, the range $\Delta x/R \approx 0.13 - 1.4$ is adopted.

The radial direction needs additional care. As previously discussed, variable thermophysical properties lead one to prefer a 1-equation model as opposed to wall functions for near-wall treatment. The discretized domain should be very fine near the wall in order to solve this equation over the laminar viscous sublayer ($y^+ < 5$). Usually the thickness of the control volume adjacent to the wall Δr_w is determinated such that the dimensionless distance y_w^+ of the centroid is approximately equal to one [98]. In this case, no ambiguity exists for calculating of physical properties since the considered point is very close to the wall. This practice allows us to estimate the thickness of the control volume adjacent to the wall as

$$\Delta r_w \approx \Delta r_w^+ = \min_x \left(\frac{2}{\sqrt{\bar{\rho}_w \, \tau_w / \mu_w^2}} \right). \tag{4.45}$$

Radially homogeneous meshes would enormously increase the computational time. For this reason, the thickness of the control volume adjacent to the axis of the mini/micro channel Δr_a is assumed much greater than previous one $\Delta r_a \gg \Delta r_w$. A geometric progression with ratio $\chi = (R - \Delta r_a)/(R - \Delta r_w)$ can be assumed to properly blend the previous extremes. The total number of elements $N_{a,w}$ depends only on extreme thicknesses, namely

$$N_{a,w} = 1 + \Xi \left\{ \frac{\ln(\Delta r_w/\Delta r_a)}{\ln\left[(R - \Delta r_a)/(R - \Delta r_w)\right]} \right\}, \tag{4.46}$$

where $\Xi : \mathbb{R} \rightarrow \mathbb{N}$ rounds the real argument to the nearest bigger natural number.

For turbulent convective heat transfer at supercritical pressure near the critical point, the condition $y_w^+ \approx 1$ is not the only one and is not the most severe. Since the easiest way to approximate the solution between two consecutive nodal values is to consider a linear function [53], an error could occur in estimating the physical properties if too coarse meshes are considered. If very high-density meshes are avoided [69], only a local grid refinement can completely solve this problem [97]. In the following, an easy strategy is proposed for this particular application in order to quickly find the proper mesh. The basic idea is to guarantee that the temperature difference between two adjacent control volumes is small enough to produce acceptable errors in estimating the maximum specific heat capacity. In the worst case, the peak of specific heat capacity is included midway between two consecutive nodal values. The minimum temperature difference ΔT_c is selected in such a way that the error for the specific heat capacity is similar to that considered in the discretization of the thermophysical database. This local constraint involves only the maximum specific heat capacity value, depends on the peak width and it may differ from ΔT_m, which derives from a global constraint. For the lowest supercritical pressure considered in this work ($74.12\ bar$), an acceptable value is $\Delta T_c \approx 2\,\Delta T_m(0.056) = 10\ mK$. If the considered calculation involves the pseudo-critical temperature, i.e. $T_0 \geq T_{pc} \geq T_w$ for cooling or $T_0 \leq T_{pc} \leq T_w$ for heating, the equation $T(x, r) = T_{pc}$ implicitly defines the pseudo-critical temperature coordinates all over the computational domain. If the pseudo-critical temperature is involved into a given transverse section of the mini/micro channel, then the radial coordinate, which identifies this temperature, is unique. The previous relation can be made explicit by considering $r = \eta(x)$. According to the assumed boundary conditions, the initial value is known $\eta\,(0) = R$. Since this function is monotonically decreasing $d_x\,\eta \leq 0$, the inverse function exists $x = \eta^{-1}(r)$. Taking advantage of this result, the local constraint can be expressed for every radial coordinate which identifies the pseudo-critical temperature within the computational domain as

$$\Delta r < \Delta r_c = \frac{\Delta T_c}{|\partial_r T(\eta^{-1}, r)|}. \tag{4.47}$$

In contrast to Eq. (4.45), the previous equation depends on the solution because the position $\eta^{-1}(r)$ of the pseudo-critical temperature is not known at the beginning.

Two main cases can be distinguished. If the axial change within the computational domain is small $|d_x \eta| \ll R/L$, then the final value does not differ consistently from the initial value $\eta(L) \approx R$. This condition is realized when small thermal fluxes at the wall or wall temperatures close to pseudo-critical temperature are considered. In this case, Eq. (4.47) can be applied for a very thin buffer region $\delta_w > R - \eta(L)$ where the grid can be homogeneously constructed finer than remaining domain. The radial discretization step can be selected by considering the most severe between the previous constraints given by Eqs. (4.45, 4.47). The remaining domain can be discretized by means of the usual geometric progression. The generic radial temperature gradient $|\partial_r T(x, r)|$ involving the pseudo-critical temperature is reported into Fig. 4.1.

Contrarily to constant property fluids, the temperature gradient is non-monotonic and a local minimum occurs for the pseudo-critical temperature at $r = \eta(x)$. In this example, which corresponds to the first validation test discussed in the following section, the pseudo-critical temperature is well confined within the buffer region $\delta_w = 20\,\Delta r_w$. It is interesting to note that $|\partial_r T(\eta^{-1}, r)|$ decreases moving away from the wall. For this reason, the critical discretization step Δr_c increases moving away from the wall. It will be more difficult to satisfy Eq. (4.47) at the inlet of the mini/micro channel because in this region the pseudo-critical temperature is located near the wall. Practically, this problem can be overcome by considering a modest forcing of the previous condition. Assuming that Eq. (4.47) is satisfied only for $x > x_c$ where

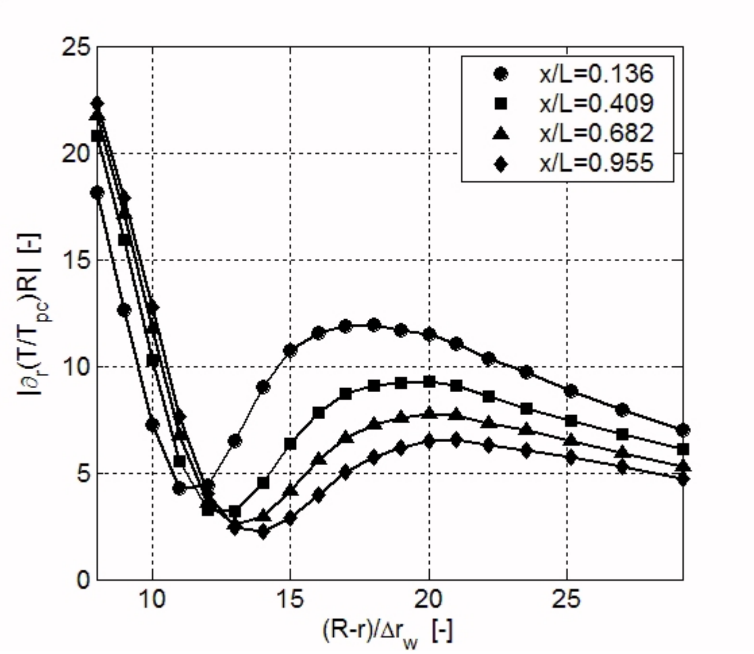

Figure 4.1: Effect of pseudo-critical temperature on radial temperature gradients at different axial locations $x/L = 0.136-0.955$. Adopted mesh is homogeneously defined for $(R-r)/\Delta r_w < 20$ and then made coarser by geometric progression.

$x_c \ll L$, i.e. only for $r < r_c$ where $R - r_c \ll \delta_w$, the limiting threshold for the radial discretization into buffer region due to the pseudo-critical temperature can be found $\Delta r_c^m = \Delta T_c \;/\; |\partial_r T(\eta_c^{-1}, r_c)|$. Considering $x_c/L = 0.136$ in the previous example, the limiting radial discretization in the buffer region due to the pseudo-critical temperature is much more severe than that given by Eq. (4.45) due to low-Reynolds turbulence models $\Delta r_c^m \,/\, \Delta r_w^+ \approx 0.129$.

If the pseudo-critical temperature radial position changes substantially within the computational domain, then the final value differs from the initial value $\eta(L) < R$ or eventually, for an axial coordinate x_a, the pseudo-critical temperature intersects the centerline $\eta(x_a) = 0$. It is not possible to define, in this case, a buffer region where the pseudo-critical temperature is confined. However, in this case the weak strategy of satisfying Eq. (4.47) only for $x > x_c$ where $x_c \ll L$ implies that the

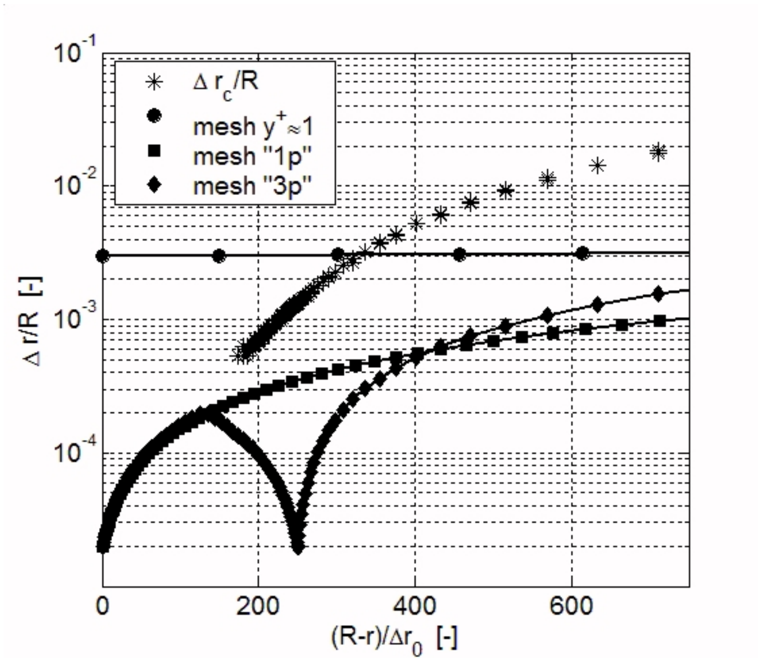

Figure 4.2: Critical discretization steps due to pseudo-critical temperature ($\Delta r_0/R = 2 \times 10^{-5}$). The limiting threshold is $\Delta r_c^m/R = 5 \times 10^{-4}$ at $x_c/L = 0.018$. Labels “1p” and “3p” refer to the number of constitutive geometric progressions.

limiting threshold for the radial discretization is located farther from the wall because $\eta_c/x_c \propto |d_x\,\eta| \gg R/L$. If the radial thickness required by the most severe threshold is the same previously considered, moving away from the wall would simply increase the high-resolution portion of the mesh. Instead $|\partial_r\, T(\eta^{-1}, r)|$ decreases moving away from the wall and for this reason the limiting threshold Δr_c^m allows us to consider coarser meshes. In Fig. 4.2 a comparison among different meshes, which refers to the experimental runs discussed in the following section, is reported, together with the critical discretization steps due to pseudo-critical temperature. Despite the fact that x_c is much smaller than the value previously considered in the first validation test $x_c/L = 0.018 \ll 0.136$, the limiting radial threshold is weaker $\Delta r_c^m/R = 5 \times 10^{-4} \gg 1 \times 10^{-5}$. Unfortunately in this case Eq. (4.47) must be satisfied for the whole computational domain and also when the radial discretization proceeds towards the centerline. The first idea is to construct a mesh characterized by higher resolution at the wall and then to verify that the geometric progression satisfies Eq. (4.47) for any radial coordinate. This strategy corresponds to the single-progression mesh reported in Fig. 4.2. If preliminary results allow us to estimate the limiting condition due to pseudo-critical temperature, multiple-progression meshes can be considered to optimally distribute nodal values along the radial direction. Also in this case, the limiting radial discretization due to pseudo-critical temperature is much more severe than that given by Eq. (4.45) due to low-Reynolds turbulence models $\Delta r_c^m \,/\, \Delta r_w^+ \approx 0.167$.

If a first estimation of the solution is given, then the previous considerations make it possible to design a refined mesh, which properly satisfies the constraints due to the pseudo-critical temperature. Since in many cases these constraints are the most severe among those that affect the solution process, usually the refined mesh ensures the mesh-independence of the solutions. Therefore, this strategy reduces to consider a couple of meshes to solve the problem: a first guess mesh to estimate the solution and a second refined mesh, which depends on how the radial position of pseudo-critical temperature changes in the computational domain, i.e. if $|d_x\,\eta| \ll R/L$ or $|d_x\,\eta| \gg R/L$. Let us consider again the first validation test, which will be presented later on. Since, in this case, the wall thermal flux is fixed, the wall temperature distribution can be used to check if the solution is mesh-independent. Since all meshes share the same axial discretization, each wall temperature distribution can be compared with the final solution by reporting the averaged value and the standard deviation of wall temperature discrepancies. A first guess mesh with 60 radial nodes and $y_w^+ \approx 1$ produces wall temperature discrepancies equal to $121.0 \pm 90.0\; mK$, which are much higher than $\Delta T_c = 10\; mK$. The problem is not overcome by simply refining the mesh at the wall: a second guess mesh with 80 radial nodes and $y_w^+ \approx 0.1$ produces wall temperature discrepancies equal to $55.0 \pm 79.0\, mK$. As previously reported for this case, if the same radial nodes are organized in such a way as to realize a buffer region which always includes the pseudo-critical temperature, the mesh performance is improved and the wall temperature discrepancies reduce to $0.5 \pm 0.4\, mK$. Hence considering 20 additional radial nodes substantially does not improve further the accuracy. The proposed strategy reduces the number of grid nodes to the minimum needed for describing properly the effects of pseudo-critical temperature. The greatest mesh used in the numerical simulations reported further on is characterized by 118 radial nodes, which are much less than those prescribed by single-progression high-density meshes [69].

Since the discretization strategy is defined, the whole resolution process can proceed. The discretized governing equations for continuity, momentum and energy are solved sequentially in order to realize a solution loop. The SIMPLE algorithm [89] is adopted. It prescribes a relationship between velocity and pressure values which enforces mass conservation and produces the pressure field. Because these equations are non-linear and highly-coupled by the dependence of thermophysical properties on temperature, several iterations of the solution loop must be performed before a converged solution is obtained. To take into account the effect of density fluctuations on turbulent diffusivities, they are corrected at the end of each iteration by means of parameter ϕ, calculated according to the turbulence models previously discussed. When all the unknown variables are updated by corrective quantities which are small enough to satisfy a given convergence criterion, the solution loop terminates. The relative convergence criterion is equal to 1×10^{-3} for the validation cases [98], which are characterized by fixed wall thermal flux, and it is equal to 1×10^{-5} for the experimental runs, which are characterized by fixed wall temperature. For each discretized equation, a Gauss-Seidel linear equation solver is used in conjunction with an algebraic multi-grid method to solve the resulting scalar system of equations for the solving variables [89]. In order to prevent divergence, the velocity components in the momentum equations, the temperature in the energy equation and the transport properties are updated by corrective quantities smaller than those due to pure calculation. The ratio between corrective quantities and those due to pure calculation is called under-relaxation factor. Near the critical point, Lee and Howell [98] suggested to iteratively renew with an under-relaxation factor the thermophysical properties too. The under-relaxation of the thermophysical properties causes the velocity and the temperature fields to respond rather slowly during solution process. This practice realizes a multi-level under-relaxation which prevents strong instabilities emerging when too coarse meshes are adopted to describe fluid flow near the critical point. If the mesh is chosen according to previously discussed strategy, there is no need for multi-level under-relaxation.

4.4 Numerical results

4.4.1 Comparison with other predictions and experimental data for the local heat transfer coefficient

The present work aims to investigate the turbulent convective heat transfer in mini/micro channels for carbon dioxide at supercritical pressure in order to numerically verify the existence of heat transfer impairment. Before proceeding in this direction, a comparison with other numerical predictions and experimental data is needed. This comparison firstly allows us to verify the reliability of numerical results and secondly to test if the proposed approach for density fluctuations is more efficient than the usual approach. The experiments oriented to characterize the convective heat transfer usually aim to measure the local heat transfer coefficient and/or the average heat transfer coefficient. Two common practices are considered. In the first case, the wall thermal flux is imposed and the measurement of the local heat transfer coefficient reduces to the measurement of the wall temperature. The wall temperature is kept fixed and the measurement of the average heat transfer coefficient is obtained from the heat balance between the wall heat flux and the bulk enthalpy increase of the fluid. In both cases, the bulk enthalpy increase is supposed much larger than changes of kinetic and potential energy or the axial heat diffusion at each end of the duct. If the local heat transfer coefficients are known, then the average heat transfer coefficient can be calculated by line integration along the axis but not vice versa. For this reason, the comparison with experimental measurements of local heat transfer coefficients is more meaningful for verifying the reliability of the numerical results. Moreover, since the numerical results will be used to discriminate among some phenomenological correlations oriented to average heat transfer coefficients, an independent validation step, which involves local heat transfer coefficients, is needed. Due to experimental difficulties, there have been few radial temperature measurements inside a tube which involve the pseudo-critical temperature. This consideration is even more true for mini/micro channels where the characteristic sizes are prohibitive ($d < 2\ mm$). For this reason, the experimental data for a normal sized duct due to Wood and Smith [99] will be considered. They considered an upward flow of carbon dioxide under heating conditions in a tube with common diameter ($d = 22.91\ mm$) and measured radial temperature profiles by keeping the wall thermal flux fixed. The same set of data has been considered for validation purposes by Lee and Howell [98]. In this case, the effect of gravity has been added to the

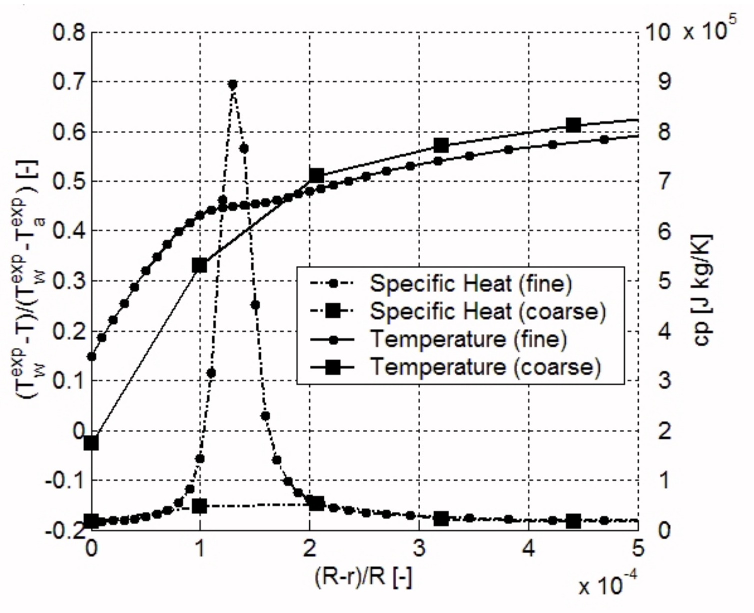

Figure 4.3: Predicted profiles for specific heat capacity and fluid temperature by meshes based on geometric progression. The coarse mesh ($y_w^+ \approx 1$) is not suitable to describe the peak in specific heat capacity.

momentum equation, since Eq. (4.1) did not hold for this case.

In Fig. 4.3 the effect of the radial discretization on the solution is reported. The mesh based on Eq. (4.45) shows to be too coarse for describing the peak of specific heat capacity. Since the concavity of the temperature profile changes because of the peak in specific heat capacity, the coarse mesh introduces some errors in predicting the temperature profile, and, consequently, the local heat transfer coefficient. In this particular case, the coarse mesh could lead us to think that the model of Bellmore and Reid works better than it really does. In this case, the radial discretization induces some errors in the wall temperature which are of the same order of magnitude of the uncertainties involved in experimental measurements. The coarse mesh shows a strong unstable behavior because the solution process tries to cut off the peak in specific heat capacity, which behaves like local numerical noise breaking the smooth solution. This probably justifies the need of multi-level under-relaxation in the numerical simulations

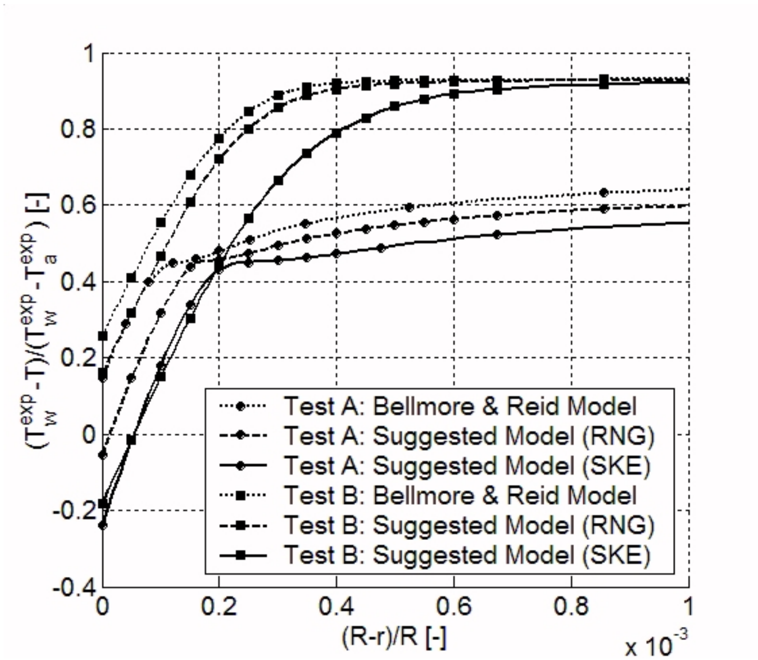

Figure 4.4: Comparison of predicted profiles of dimensionless temperature calculated by means of different models for experimental configurations considered by Wood and Smith [99] (63.05 kW/m^2 for $Test\ A$ and 204.91 kW/m^2 for $Test\ B$). The label "RNG" means RNG $k-\epsilon$ model and the label "SKE" means standard $k-\epsilon$ model.

performed by Lee and Howell [98]. In the following only fine meshes will be considered.

A comparison of predicted profiles of dimensionless temperature calculated by means of different models with experimental data by Wood and Smith [99] in a thin layer near the wall is shown in Fig. 4.4. The reported cases are different because of the wall thermal flux, which is 63.05 kW/m^2 for $Test\ A$ and 204.91 kW/m^2 for $Test\ B$. Because of the high mass flow rate ($Re = 9.3 \times 10^5$), the pseudo-critical temperature is positioned near the wall and it is well confined within a small buffer region. In both tests the model of Bellmore and Reid underestimates the wall temperature $T_w < T_w^{exp}$. This result partially contradicts the conclusion of Lee and Howell [98], which was probably due to the previously discussed effects of discretization. The proposed approach for taking into account the effects of density fluctuations has been applied together with both the standard $k-\epsilon$ model and the RNG $k-\epsilon$ model. In

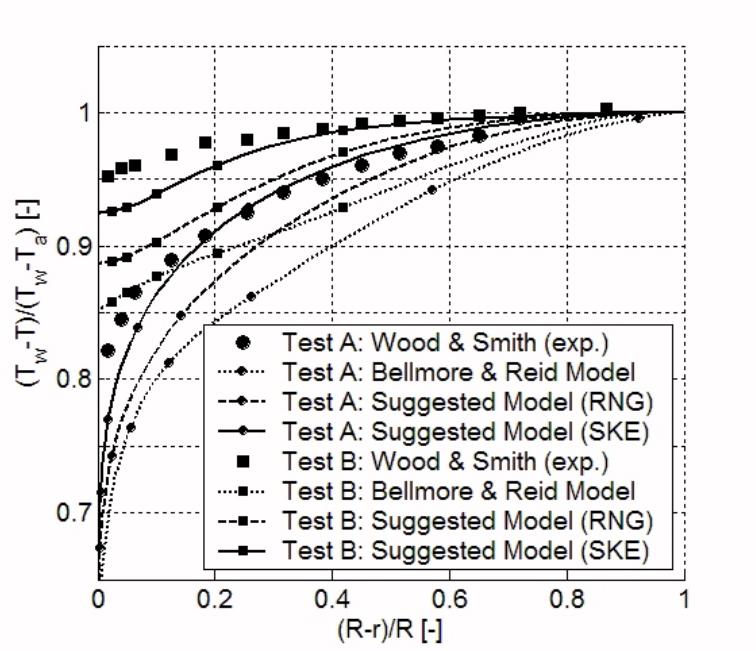

Figure 4.5: Comparison of predicted profiles of dimensionless temperature calculated by means of different models with experimental data of Wood and Smith [99] (63.05 kW/m^2 for $Test\ A$ and 204.91 kW/m^2 for $Test\ B$).

both tests the standard $k-\epsilon$ model overestimates the wall temperature $T_w > T_w^{exp}$. On the other hand, the RNG $k-\epsilon$ model produces the best results and this is even more true for the smallest wall thermal flux. For this application, the RNG $k-\epsilon$ model improves the near-wall description by taking into account the low-Reynolds-number effects [89]. The proposed approach allows formulating numerical predictions of wall temperature which differ from experimental data by $\pm 20\,\%$. This threshold allows us to discriminate among different phenomenological correlations. It is interesting to note that the experimental datum is approximately located midway into the uncertainty range due to turbulence closure models.

In order to complete the comparison of the predicted dimensionless temperature profiles with experimental data by Wood and Smith [99], the whole radial profiles are reported into Fig. 4.5. The numerical predictions due to the proposed approach are in

Table 4.1: Comparison among numerical predictions of local heat transfer coefficients, experimental data of Wood and Smith [99] (label "W&S") and other numerical predictions of Lee and Howell [98] (label "L&H"). The considered models are: the model of Bellmore and Reid [86] (label "B&R"); the RNG $k-\epsilon$ model (label "RNG") and the standard $k-\epsilon$ model (label "SKE"). The best results are bold-faced.

Test A: $q_w = 63.05\ kW/m^2$, $T_b = 302.82\ K$, $Re = 9.3 \times 10^5$

Parameters	W&S (Exp.)	L&H (B&R)	This Work (B&R)	This Work (RNG)	This Work (SKE)
$T_w\,[K]$	305.76	305.60	305.29	305.94	306.51
$\alpha\,[kW/m^2K]$	21.45	23.88	25.53	20.21	17.09
e_α [%]	± 20 %	+11.3	+19.0	**−5.8**	−20.3

Test B: $q_w = 204.91\ kW/m^2$, $T_b = 303.15\ K$, $Re = 9.3 \times 10^5$

Parameters	W&S (Exp.)	L&H (B&R)	This Work (B&R)	This Work (RNG)	This Work (SKE)
$T_w\,[K]$	327.37	323.20	320.97	323.38	331.88
$\alpha\,[kW/m^2K]$	8.46	10.62	11.50	10.13	7.13
e_α [%]	± 20 %	+25.5	+35.9	+19.7	**−15.7**

good agreement with the experimental data. In both tests the standard $k-\epsilon$ model better reproduces the dimensionless temperature profile in the bulk region. Despite the fact that in this case the local heat transfer coefficient is mainly affected by wall temperature, this result leads one to consider in the following both the 2-equation models, such as to better describe the turbulent diffusivities. This practice is confirmed by another reason. The final goal of this section is to estimate the local heat transfer coefficient $\alpha = q_w/(T_w - T_b)$, which is conventionally positive under heating conditions. If the wall thermal flux is imposed, then only the wall temperature T_w depends on the calculation because the bulk temperature T_b is unambiguously determined by the inlet temperature T_0 and by the wall thermal flux q_w. This does not mean that the model, which better reproduces the wall temperature, will necessarily ensure the lowest error on local heat transfer coefficient. Let us introduce the numerical error on wall temperature as $e_w = (T_w^{exp} - T_w)/(T_w^{exp} - T_b)$ and the numerical error on local heat transfer coefficient as $e_\alpha = (\alpha - \alpha^{exp})/\alpha^{exp}$. Since $|e_w| \ll 1$, then the numerical error on local heat transfer coefficient e_α can be developed near zero, yielding

$$e_\alpha = \frac{e_w}{1 - e_w} = e_w + e_w^2 + O\,(e_w^3). \tag{4.48}$$

This means that the numerical models which overestimate the wall temperature, i.e. which are characterized by $e_w < 0$, induce smaller errors on the local heat transfer coefficient than the numerical models which underestimate it by the same absolute quantity $e_w > 0$. This conclusion simplifies the matching of standard $k - \epsilon$ model with experimental data because it usually overestimates the wall temperature. If the difference between performances of these models is small, then this conclusion must be taken into account to estimate local heat transfer coefficients. In Tab. 4.1, the predicted values for both wall temperatures and local heat transfer coefficients are reported. For $Test\ B$, despite the fact that the RNG $k - \epsilon$ model works better to predict the wall temperature than the standard $k - \epsilon$ model $|e_w^{RNG}| < |e_w^{SKE}|$, the conclusion on local heat transfer coefficient is exactly the opposite $|e_\alpha^{RNG}| > |e_\alpha^{SKE}|$. In the following calculations, both RNG $k - \epsilon$ model and standard $k - \epsilon$ model will be considered.

4.4.2 Comparison with other predictions and experimental data for the average heat transfer coefficient

In this section, the discussed models will be adopted to predict heat transfer under cooling conditions in mini/micro channels for carbon dioxide at supercritical pressure.

The numerical results will be compared with some phenomenological correlations for estimating the average heat transfer coefficients. Since these correlations generally produce conflicting predictions, it would be interesting to determine if the numerical results systematically show better agreement with a particular correlation. These calculations could help to settle the controversy on the existence of a heat transfer impairment in mini/micro channels in comparison with normal-sized ducts. In all these calculations, the effects due to the gravity field have been purposely excluded in order to verify if buoyancy is responsible for heat transfer impairment. The basic problem is to decide what pattern of test conditions will best reveal the aspects of the investigated phenomena and will make possible a meaningful comparison with phenomenological correlations. This is a typical example of experimental design [41].

For the present application, there are five factors usually considered by all phenomenological correlations: the working pressure p; the bulk temperature $T_b(x)$; the wall temperature $T_w(x)$; the diameter of mini/micro channel d and finally the mass flow rate, G. In the experimental runs, the wall temperature $T_w(x) = T_w$ will be assumed uniformly distributed along the axial direction and the final goal will be the calculation of the wall thermal flux $q_w(x)$. According to this strategy, the inlet bulk temperature $T_b(0) = T_0$ is a selectable factor. As previously discussed, the numerical prediction of turbulent convective heat transfer involves some proper hypotheses for describing turbulence: the turbulence model M completes the set of factors. For the present application, the average heat transfer coefficient can be considered as the response. Unfortunately the definition of the average heat transfer coefficient is not unique because it is essentially conventional. Let us define α_L^* the heat transfer coefficient due to a generic definition. All the definitions share the same feature of reproducing the local heat transfer coefficient as a limit, i.e. $\lim_{L\to 0} \alpha_L^* = \alpha$. In the present work, the following definition will be adopted

$$\alpha_L = \frac{\left(\int_0^L q_w \, dx\right)/L}{\left(\theta_0 - \theta_L\right)/\ln\left(\theta_0/\theta_L\right)}, \tag{4.49}$$

where $\theta_0 = T_b(0) - T_w$ and $\theta_L = T_b(L) - T_w$. The strong dependence of the specific heat capacity on temperature near the critical point precludes the possibility of applying some elementary heat transfer models but it does not prevent one to define a logarithmic mean temperature difference. The adopted definition for the average heat transfer coefficient α_L generally differs from those adopted by phenomenological correlations α_L^*. For this reason, the direct comparison between α_L and α_L^* would be spurious because affected by both experimental content and differing definitions. In the present work, when a comparison between a numerical result and a phenomenological correlation is needed, the mini/micro channel is axially discretized into infinitesimal portions with length dL and within each one of them the limit value $\alpha \approx \lim_{L\to dL} \alpha_L^*$ for local heat transfer coefficient is considered. Finally, a coefficient coherent with Eq. (4.49) but due to the considered phenomenological correlation is calculated. In this way, the comparison is made on the basis of the same definition for the average heat transfer coefficient.

The main trends of response can be usually investigated by means of only two levels. Concerning pressure, this means that a slightly supercritical pressure and a much higher pressure are considered. Concering bulk temperature, the levels should allow us to take into account the effects of pseudo-critical temperature but, in this case, two levels are not enough. Let us consider the following function defined as

$$c_p^w(T) = \frac{1}{T - T_w} \int_{T_w}^{T} \overline{h}(T,p)\, dT. \tag{4.50}$$

The previous quantity allows us to define the specific heat capacity at the wall $c_p^{ww} = \lim_{T\to T_w} c_p^w(T)$ and the average specific heat capacity $c_p^{wb} = c_p^w(T_b)$. Many authors agree on the importance of the ratio c_p^{wb}/c_p^{ww} between the average and the wall specific heat capacity to characterize heat transfer near the critical point [71, 75, 77]. Obviously this means that heat transfer depends on the eventual presence of the pseudo-critical temperature in the range defined by wall and bulk conditions. Moreover, this means that a configuration with the wall temperature close to the pseudo-critical value is not equivalent to a configuration with the bulk temperature close to the pseudo-critical value. These configurations are different because of the distortion of the radial temperature profile. Practically, the ratio c_p^{wb}/c_p^{ww} discriminates the cases characterized by $T_b(x) \approx T_{pc}$, which implies $c_p^{wb} > c_p^{ww}$, and the other case characterized by $T_w(x) \approx T_{pc}$, which implies $c_p^{wb} < c_p^{ww}$. The factorial design must take into account both configurations, too. Three inlet bulk temperatures are selected: the first very close to the pseudo-critical value $T_0 \approx T_{pc}$; the second, higher than previous one, so that the wall temperature can be close to the pseudo-critical value $T_w \approx T_{pc}$ and the third much higher. Concerning wall temperature, two levels are always considered and the difference $T_0 - T_w$ is increased far from the pseudo-critical temperature where heat transfer is weaker. Since the effects due to gravity field are neglected, Eq. (4.1) allows us to reduce the number of free parameters. The buoyancy parameter can be factorized $Gr/Re_0^2 = Bo_T\ Bo_G$. The first term Bo_T depends on both bulk and wall temperature, while the second term Bo_G depends on the mini/micro channel diameter and the mass flow rate, namely

$$Bo_T = \frac{\rho_w \rho_0 - \rho_0^2}{\rho_{pc}^2}, \tag{4.51}$$

$$Bo_G = \frac{\pi^2}{16}\,\frac{g \rho_{pc}^2 d^5}{G^2}. \tag{4.52}$$

Since the selected factorial design implies $Bo_T \leq 6.09 \times 10^{-1}$, Eq. (4.1) reduces to $Bo_G \leq 1.64 \times 10^{-3}$. In the following $Bo_G = 1.31 \times 10^{-3}$ is assumed and two levels for the mini/micro channel diameter ($d < 2\ mm$), or equivalently two levels for the mass flow rate, are selected. Finally, three turbulence models are included: the approach of Bellmore and Reid and the proposed approach, together with both the RNG $k-\epsilon$ model and the standard $k-\epsilon$ model. The previous assumptions define a simplified $2 \times 3 \times 2 \times 2 \times 3$ factorial design [41], which requires 72 runs.

The numerical predictions of the average heat transfer coefficient α_L are grouped by means of the selected levels for the supercritical pressure and the diameter of the mini/micro channel: in Tab. 4.2 the experimental runs $\#1-18$; in Tab. 4.3 the experimental runs $\#19-36$; in Tab. 4.4 the experimental runs $\#37-54$ and finally in Tab. 4.5 the experimental runs $\#55-72$. Before proceeding to compare these results with experimental data and other numerical predictions, a sensitivity analysis of the considered factors is reported. As for turbulence description, the standard $k-\epsilon$ model systematically produces lower values for the average heat transfer coefficient in comparison with the RNG $k-\epsilon$ model. In the previous section, the fact that the standard $k-\epsilon$ model overestimates the effective temperature difference $|T_b - T_w|$ has been already pointed out and it is consistent with the present results. Usually the average heat transfer coefficients predicted by the RNG $k-\epsilon$ model are slightly lower than those due to the model of Bellmore and Reid, with the exception of the experimental runs which are characterized by $T_0 \approx T_{pc}$ and which reveal a reverse trend. When the pseudo-critical temperature is close to bulk temperature, the radial temperature profile is distorted and it looks similar to a step function. Near the wall this feature implies a rapidly strained flow, which enhances the generation of turbulence kinetic energy. The additional terms, which are included in the RNG $k-\epsilon$ model to describe rapidly strained flows, probably justifies the increase in the predicted values of the average heat transfer coefficient. Concerning the inlet temperature difference

Table 4.2: Numerical predictions of average heat transfer coefficient α_L for experimental runs #1 − 18 defined by the factorial design. The lowest supercritical pressure (7.412 MPa) and the smallest mini/micro channel diameter (0.787 mm) are considered. The adopted models are: the model of Bellmore and Reid [86] (label "B&R"); the RNG $k - \epsilon$ model (label "RNG") and the standard $k - \epsilon$ model (label "SKE"). The pseudo-critical temperature is $T_{pc} = 304.328\ K$.

	Factorial Design						Results		
#	p $[MPa]$	T_0 $[K]$	T_w $[K]$	d $[mm]$	(G) $[g/s]$	M	q_w $[kW/m^2]$	$\|\Delta T_b\|$ $[K]$	α_L $[kW/m^2K]$
1	7.412	305	302	0.787	0.571	B&R	111.92	0.69	42.359
2	7.412	305	302	0.787	0.571	RNG	115.57	0.69	43.803
3	7.412	305	302	0.787	0.571	SKE	99.38	0.67	37.519
4	7.412	305	298	0.787	0.571	B&R	172.60	1.97	28.955
5	7.412	305	298	0.787	0.571	RNG	176.55	2.19	30.244
6	7.412	305	298	0.787	0.571	SKE	159.10	1.38	25.307
7	7.412	312	309	0.787	0.571	B&R	18.71	2.33	12.004
8	7.412	312	309	0.787	0.571	RNG	17.52	2.19	10.484
9	7.412	312	309	0.787	0.571	SKE	15.91	2.01	8.772
10	7.412	312	305	0.787	0.571	B&R	58.35	5.65	16.991
11	7.412	312	305	0.787	0.571	RNG	54.49	5.41	14.972
12	7.412	312	305	0.787	0.571	SKE	48.65	5.02	12.236
13	7.412	360	353	0.787	0.571	B&R	17.55	6.01	5.704
14	7.412	360	353	0.787	0.571	RNG	16.76	5.74	5.013
15	7.412	360	353	0.787	0.571	SKE	15.87	5.44	4.383
16	7.412	360	340	0.787	0.571	B&R	50.23	16.56	5.344
17	7.412	360	340	0.787	0.571	RNG	49.86	16.47	5.243
18	7.412	360	340	0.787	0.571	SKE	47.12	15.60	4.575

Table 4.3: Numerical predictions of average heat transfer coefficient α_L for experimental runs #$19-36$ defined by the factorial design. The lowest supercritical pressure (7.412 MPa) and the biggest mini/micro channel diameter (1.417 mm) are considered. The adopted models are: the model of Bellmore and Reid [86] (label "B&R"); the RNG $k-\epsilon$ model (label "RNG") and the standard $k-\epsilon$ model (label "SKE"). The pseudo-critical temperature is $T_{pc} = 304.328\ K$.

	Factorial Design						Results		
#	p $[MPa]$	T_0 $[K]$	T_w $[K]$	d $[mm]$	(G) $[g/s]$	M	q_w $[kW/m^2]$	$\|\Delta T_b\|$ $[K]$	α_L $[kW/m^2K]$
19	7.412	305	302	1.417	2.482	B&R	131.49	0.63	49.242
20	7.412	305	302	1.417	2.482	RNG	162.26	0.66	61.020
21	7.412	305	302	1.417	2.482	SKE	134.35	0.64	50.341
22	7.412	305	298	1.417	2.482	B&R	231.75	0.67	34.806
23	7.412	305	298	1.417	2.482	RNG	280.40	0.70	42.188
24	7.412	305	298	1.417	2.482	SKE	239.90	0.67	36.035
25	7.412	312	309	1.417	2.482	B&R	26.47	1.43	11.968
26	7.412	312	309	1.417	2.482	RNG	26.22	1.41	11.813
27	7.412	312	309	1.417	2.482	SKE	22.94	1.22	9.875
28	7.412	312	305	1.417	2.482	B&R	79.42	3.75	16.256
29	7.412	312	305	1.417	2.482	RNG	80.34	3.79	16.522
30	7.412	312	305	1.417	2.482	SKE	69.42	3.67	13.521
31	7.412	360	353	1.417	2.482	B&R	27.84	3.98	5.879
32	7.412	360	353	1.417	2.482	RNG	26.89	3.85	5.574
33	7.412	360	353	1.417	2.482	SKE	24.43	3.50	4.838
34	7.412	360	340	1.417	2.482	B&R	82.92	11.54	6.183
35	7.412	360	340	1.417	2.482	RNG	79.99	11.15	5.850
36	7.412	360	340	1.417	2.482	SKE	72.80	10.18	5.088

Table 4.4: Numerical predictions of average heat transfer coefficient α_L for experimental runs $\#37-54$ defined by the factorial design. The highest supercritical pressure (12.0 MPa) and the smallest mini/micro channel diameter (0.787 mm) are considered. The adopted models are: the model of Bellmore and Reid [86] (label "B&R"); the RNG $k-\epsilon$ model (label "RNG") and the standard $k-\epsilon$ model (label "SKE"). The pseudo-critical temperature is $T_{pc} = 327.1\ K$.

	Factorial Design						Results		
#	p $[MPa]$	T_0 $[K]$	T_w $[K]$	d $[mm]$	(G) $[g/s]$	M	q_w $[kW/m^2]$	$\lvert\Delta T_b\rvert$ $[K]$	α_L $[kW/m^2K]$
37	12.000	327	317	0.787	0.571	B&R	67.21	6.78	11.232
38	12.000	327	317	0.787	0.571	RNG	70.36	7.13	12.322
39	12.000	327	317	0.787	0.571	SKE	64.91	6.53	10.518
40	12.000	327	307	0.787	0.571	B&R	133.53	15.18	12.519
41	12.000	327	307	0.787	0.571	RNG	132.12	14.98	12.189
42	12.000	327	307	0.787	0.571	SKE	123.04	13.70	10.374
43	12.000	347	337	0.787	0.571	B&R	52.14	8.08	10.658
44	12.000	347	337	0.787	0.571	RNG	49.65	7.75	9.549
45	12.000	347	337	0.787	0.571	SKE	45.76	7.21	8.097
46	12.000	347	327	0.787	0.571	B&R	112.99	15.24	10.641
47	12.000	347	327	0.787	0.571	RNG	118.00	15.75	11.606
48	12.000	347	327	0.787	0.571	SKE	108.26	14.75	9.815
49	12.000	360	353	0.787	0.571	B&R	25.11	5.54	7.101
50	12.000	360	353	0.787	0.571	RNG	25.22	5.56	7.176
51	12.000	360	353	0.787	0.571	SKE	23.58	5.22	6.181
52	12.000	360	340	0.787	0.571	B&R	81.61	16.01	8.214
53	12.000	360	340	0.787	0.571	RNG	82.68	16.18	8.460
54	12.000	360	340	0.787	0.571	SKE	76.88	15.23	7.237

Table 4.5: Numerical predictions of average heat transfer coefficient α_L for experimental runs #$55 - 72$ defined by the factorial design. The highest supercritical pressure (12.0 MPa) and the biggest mini/micro channel diameter (1.417 mm) are considered. The adopted models are: the model of Bellmore and Reid [86] (label ”B&R”); the RNG $k - \epsilon$ model (label ”RNG”) and the standard $k - \epsilon$ model (label ”SKE”). The pseudo-critical temperature is $T_{pc} = 327.1\ K$.

	Factorial Design						Results		
#	p $[MPa]$	T_0 $[K]$	T_w $[K]$	d $[mm]$	(G) $[g/s]$	M	q_w $[kW/m^2]$	$\|\Delta T_b\|$ $[K]$	α_L $[kW/m^2K]$
55	12.000	327	317	1.417	2.482	B&R	103.21	4.18	13.367
56	12.000	327	317	1.417	2.482	RNG	109.08	4.43	14.411
57	12.000	327	317	1.417	2.482	SKE	95.39	3.85	12.048
58	12.000	327	307	1.417	2.482	B&R	219.42	9.52	14.898
59	12.000	327	307	1.417	2.482	RNG	213.88	9.25	14.354
60	12.000	327	307	1.417	2.482	SKE	189.73	8.07	12.147
61	12.000	347	337	1.417	2.482	B&R	84.63	5.67	12.489
62	12.000	347	337	1.417	2.482	RNG	76.78	5.18	10.821
63	12.000	347	337	1.417	2.482	SKE	67.98	4.63	9.128
64	12.000	347	327	1.417	2.482	B&R	177.25	10.18	12.753
65	12.000	347	327	1.417	2.482	RNG	184.83	11.20	13.545
66	12.000	347	327	1.417	2.482	SKE	162.97	10.09	11.340
67	12.000	360	353	1.417	2.482	B&R	43.97	4.07	9.410
68	12.000	360	353	1.417	2.482	RNG	39.62	3.68	8.033
69	12.000	360	353	1.417	2.482	SKE	35.58	3.32	6.890
70	12.000	360	340	1.417	2.482	B&R	130.84	11.27	9.622
71	12.000	360	340	1.417	2.482	RNG	130.56	11.25	9.592
72	12.000	360	340	1.417	2.482	SKE	116.80	10.18	8.162

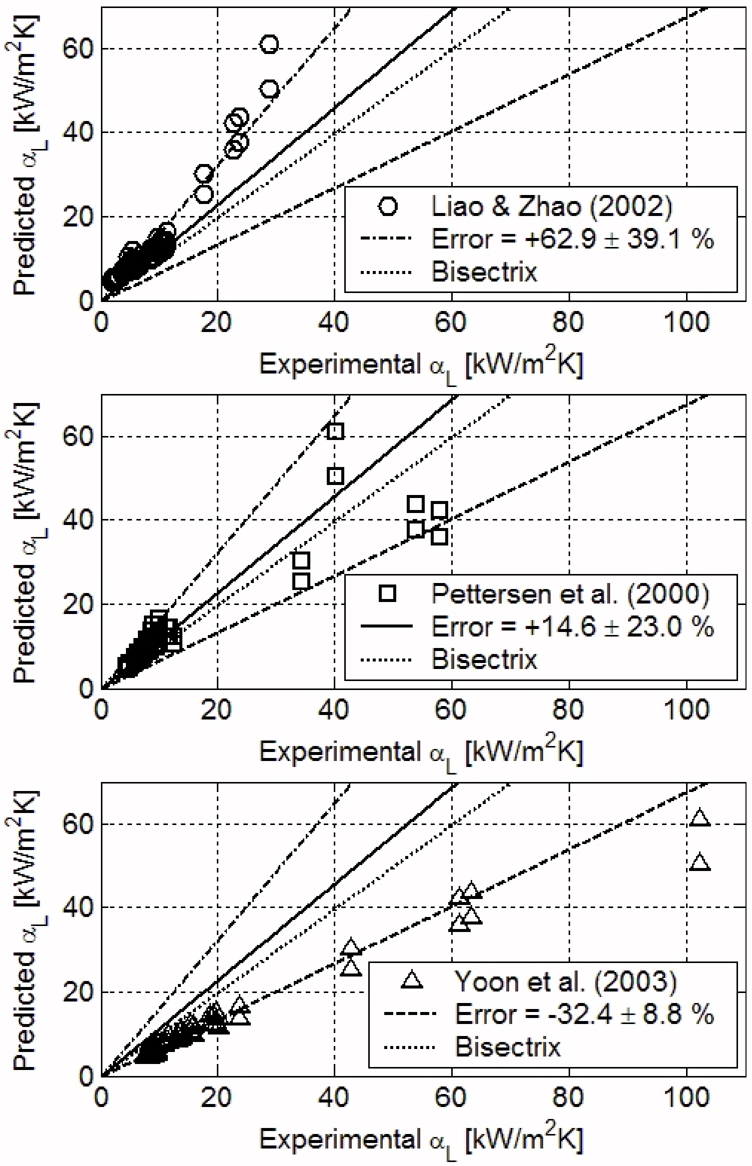

Figure 4.6: Average heat transfer coefficients obtained by both the RNG $k-\epsilon$ model and the standard $k-\epsilon$ model are jointly reported, in order to duplicate the predictions for the same run. Some phenomenological correlations are considered [73, 75, 77]. For each subplot, the numerical error due to comparison with a phenomenological correlation is reported too, in terms of mean value and standard deviation.

Table 4.6: Comparison among numerical predictions of the average heat transfer coefficients, some phenomenological correlations [73–75, 77] and other numerical predictions [72]. The considered models are: the model of Bellmore and Reid [86] (label "B&R"); the RNG $k-\epsilon$ model (label "RNG") and the standard $k-\epsilon$ model (label "SKE").

	Numerical Predictions Mean ± Standard Deviation $e^L_\alpha = (\alpha_L - \alpha_L^{exp})/\alpha_L^{exp}$ [%]			
Experimental Correlations	Petrov & Popov Correlation	This work B&R	RNG	SKE
Liao & Zhao	50.6 ± 34.6	79.1 ± 48.3	76.2 ± 39.2	49.7 ± 34.8
Pettersen et al.	6.7 ± 25.4	25.9 ± 27.1	24.1 ± 23.3	5.1 ± 18.6
Pitla et al.	8.0 ± 36.1	25.5 ± 23.7	25.4 ± 31.7	6.3 ± 25.9
Yoon et al.	-37.6 ± 6.2	-25.8 ± 11.8	-26.8 ± 7.4	-37.9 ± 6.2

$|T_0 - T_w|$, the location of the pseudo-critical temperature plays an important part. The experimental runs #4 and #10 (see Tab. 4.2) share the same inlet temperature difference $|T_0 - T_w| = 7\ K$ but for the first run $T_b(0) \approx T_{pc}$, which implies $c_p^{wb}/c_p^{ww} = 3.94$, while for the second run $T_w \approx T_{pc}$, which implies $c_p^{wb}/c_p^{ww} = 0.35$. The effect on the average heat transfer coefficient is impressive: $\alpha_L = 28.96\ kW/m^2K$ for the experimental run #4 and $\alpha_L = 16.99\ kW/m^2K$ for the experimental run #10. This confirms the common practice to include the ratio c_p^{wb}/c_p^{ww} in the phenomenological correlations and to assign it a positive exponent interpolating the experimental data. Concerning the diameter of the mini/micro channel, or equivalently the mass flow rate, the factorial design is based on the assumption to keep the parameter Bo_G, given by Eq. (4.52), fixed so as to satisfy the threshold which allows us to neglect the buoyancy effects. This means that G^2/d^5 is constant and then the inlet bulk velocity $u_0 \propto G/d^2 \propto d^{1/2}$ modestly increases by doubling the diameter of mini/micro channel. For this reason, the effects on the average heat transfer coefficients are relatively modest too. Concering the supercritical pressure, the peak of the specific heat capacity at the pseudo-critical temperature enhances the convective heat transfer and the enhancement is proportional to the magnitude of the peak. The experimental runs #19 (see Tab. 4.3) and #55 (see Tab. 4.5) are both characterized by $T_b(0) \approx T_{pc}$, so that $c_p^{wb}/c_p^{ww} > 1$. The effective temperature difference for the first experimental run $|T_0 - T_w| = 3\ K$ is smaller than the one for the second experimental run $|T_0 - T_w| = 10\ K$. In spite of this, the predicted wall thermal fluxes are comparable: $q_w = 131.5\ kW/m^2$ for the experimental run #19 and $q_w = 103.21\ kW/m^2$ for the experimental run #55. The reason is due to the magnitude of the peak of the specific heat capacity at different supercritical pressures. The lowest supercritical pressure, considered by the first experimental run, causes the specific heat capacity to strongly change in the radial direction ($c_p^{wb}/c_p^{ww} = 4.62$) while the highest supercritical pressure is much less effective in doing the same ($c_p^{wb}/c_p^{ww} = 1.17$).

In Tab. 4.6 the numerical results are compared with other numerical predictions and some phenomenological correlations. The correlation proposed by Petrov and Popov [72] is included within the numerical results, because it was developed by interpolation of some numerical simulations. At least for the selected factorial design, this correlation reasonably agrees with the results due to the proposed approach, if the standard $k - \epsilon$ model is adopted. The model of Bellmore and Reid, the model assumed by Petrov and Popov and finally the proposed approach differ each other with reference to: how the variable thermophysical properties affect the common turbulent terms due to time averaging; how the turbulent terms can be calculated in terms of solving variables and how the the additional turbulent terms due to density fluctuations are described. In spite of this, the proposed approach reasonably reproduces both the previous models if the RNG $k - \epsilon$ model or the standard $k - \epsilon$ model are assumed. This means that the proposed approach is general enough to include different models independently developed. As it will be clear later on, some of the additional topics included in this work produce moderate effects on the average heat transfer coefficient and this could hide additional discrepancies among the models. In Tab. 4.6, the experimental correlations due to Liao and Zhao [75], Pettersen et al. [73], Pitla et al. [74] and Yoon et al. [77] are considered too. The first correlation was specifically developed for a single mini/micro channel. The second one derives from some experimental tests on a flat extruded tube, which involves many mini/micro channels along axial directions. The correlation of Pitla et al. improves the previous one by averaging the results obtained with constant properties evaluated at the wall and bulk temperature. Unfortunately this practice shifts the peak of the average heat transfer coefficient from the pseudo-critical temperature. This result is not confirmed by any theoretical explanation and it distinguishes this correlation from all other ones. Finally the correlation of Yoon et al. has been recently developed for normal-sized ducts. First of all, the numerical results seem to show that the buoyancy effects are not completely responsible for heat transfer impairment measured by Liao and Zhao for mini/micro channels. Despite the fact that the gravity field is completely neglected by numerical simulations, the final predictions systematically overestimate the results due to the correlation of Liao and Zhao. This conclusion is independent of the turbulence model selected. If the experimental data are reliable, some additional terms must be included into the model to justify the heat transfer impairment for mini/micro channels. If a preference among phenomenological correlations on the basis of numerical results is needed, the results due to the RNG $k-\epsilon$ model and the standard $k-\epsilon$ model can be grouped together. In Fig. 4.6 the grouped numerical results are compared with the phenomenological correlations. The

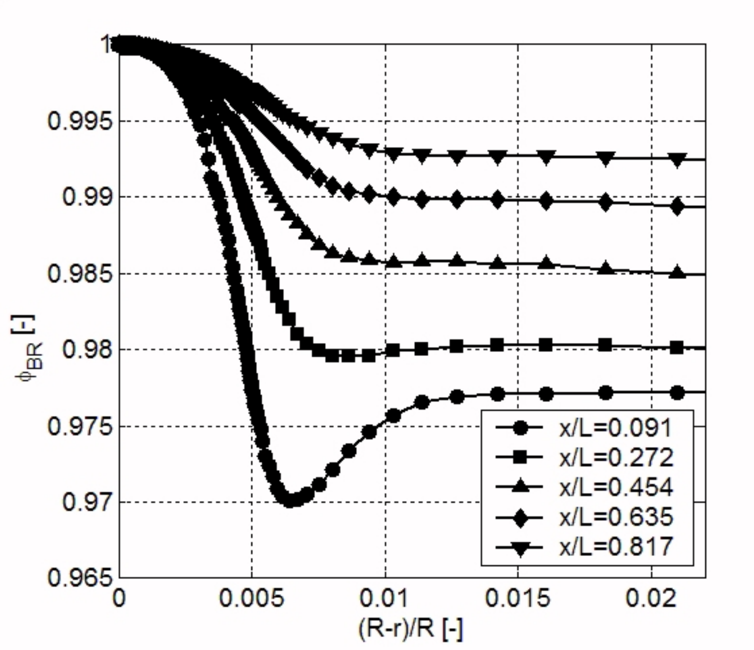

Figure 4.7: Radial profile of the corrective factor for turbulent diffusivities due to density fluctuations in a thin layer near the wall, according to the model of Bellmore and Reid [86].

grouped results seem to express a preference for the correlation proposed by Pettersen et al. [73]. This result is not conclusive because the experimental measurements for a single mini/micro channels should be more reliable than the measurements for a flat extruded tube, which can involve up to 25 mini/micro channels and can be characterized by inhomogeneities for wall temperature. However, the numerical predictions reported in the previous chapter show that the transverse inhomogeneities for a flat extruded tube are much smaller than could have been initially supposed.

Some concluding remarks on additional turbulent terms due to time averaging of density fluctuations are discussed. In Fig. 4.7 the corrective factor for turbulent diffusivities due to density fluctuations is reported. According to the assumed boundary conditions, the transverse sections of a mini/micro channel closer to the inlet are characterized by stronger radial temperature gradients. This means they have higher

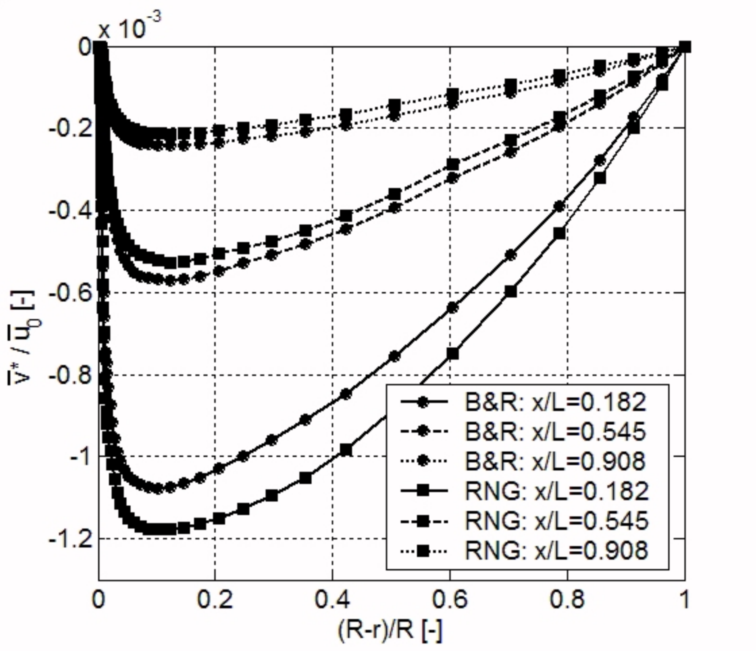

Figure 4.8: Normalized radial component of the characteristic velocity for density fluctuations at the same locations, according to different models ("B&R" means the model of Bellmore and Reid, "RNG" means the RNG $k - \epsilon$ model).

indexes of intensity for density fluctuations σ_{BR} and consequently more effective corrective factors for turbulent diffusivities ϕ_{BR}. Nevertheless, the maximum correction reported in Fig. 4.7 is less than 3 %. This threshold is even smaller for the proposed approach because $|\phi - 1| \ll |\phi_{BR} - 1|$, as previously discussed. For the present application, this correction on turbulent diffusivities produces moderate effects on the average heat transfer coefficients and this prevents a complete comparison among discussed models. In Fig. 4.8 some results are reported for radial component of the characteristic velocity for density fluctuations, according to different models. The formal expression of the radial component of the characteristic velocity for both models is the same $\overline{v}^* = \overline{v}^*_{BR}$, as it can be easily verified by considering Eqs. (4.41, 4.44). An estimation of the axial component of the characteristic velocity can be obtained by means of the radial component for both the models, recalling that $\overline{u}^* \ll \overline{u}^*_{BR} = \overline{v}^*_{BR}$.

The RNG $k-\epsilon$ model overestimates the radial component modulus of the characteristic velocity for the sections closer to the inlet, while it underestimates the same quantity proceeding along the mini/micro channel. Also in this case, the additional terms, which are included in the RNG $k-\epsilon$ model to describe rapidly strained flows, probably justify this increase in the radial component of the characteristic velocity for more distorted temperature profiles. Despite the fact that density fluctuations strongly affect the radial velocity component, as it is evident recalling that $\overline{v} \approx -\overline{v}^*$, the final result on the average heat transfer coefficients is quite moderate.

4.5 Conclusions

A new approach to take into account the effects on turbulence of variable physical properties due to closeness to the critical point has been proposed, by generalizing the decomposition originally considered by the model of Bellmore and Reid. This approach allows us to freely choose the turbulence model for usual terms coming from time averaging of velocity fluctuations and to describe coherently the additional terms due to density fluctuations. In this way, the turbulence due to density fluctuations is analyzed from a general point of view, which imposes no constraint on the remainder of the model.

Numerical calculations based on the proposed approach and on the original model have been performed for carbon dioxide flowing within mini/micro channels under cooling conditions. In comparison with existing calculations, some improvements have been considered: an updated database for thermophysical properties near the critical point; some differential equations to investigate the effects of variable thermophysical properties on turbulence; different turbulence closure models for usual terms and for additional terms due to density fluctuations. These refinements do not substantially improve the existing results. This means that for the considered application the effects due density fluctuations are smaller than it could have been initially supposed on the basis of some interpretations [75]. The comparison with phenomenological correlations confirms that a heat transfer impairment for mini/micro channels exists but it is smaller than the impairment which has been measured by some experimental investigations for the same devices. The results are not completely exhaustive because of the discrepancies among different correlations. The strong coupling between heat transfer and fluid flow due to variable thermophysical properties complicates the development of a reliable correlation in terms of traditional dimensionless parameters. For this reason, some recent attempts [100] to adopt a neural network regression technique in order to interpolate the experimental results concerning the convective heat transfer near the critical point appear greatly promising.

In this chapter, some heuristic decompositions for the additional unknown quantities which derive from time-averaging the instantaneous conservation equations of mass, momentum and energy have been discussed. Time-averaging the instantaneous conservation equations produces the so-called Reynolds-averaged Navier-Stokes (RANS) equations. Neglecting the possibility of directly solving the instantaneous conservation equations, a more fundamental approach can netherless be formulated. The basic idea lies in filtering the instantaneous Navier-Stokes equations in either Fourier (wave-number) space or configuration (physical) space [81]. The filtering process effectively filters out the eddies whose scales are smaller than the filter width or grid spacing used in the computations. However, also in this case a new closure problem arises because a subgrid model is needed in order to calculate the additional filtered quantities in terms of solved variables. Recently, a pioneering paper has investigated the possibility to apply a mean-field approach (filtering out subgrid scales) to the Boltzmann equation in order to derive a subgrid turbulence model based on kinetic theory [101]. The basic idea is that the filtering operation and going to the hydrodynamic limit are two distinct operations which do not commute, because kinetic fluctuations generally do not annihilate upon filtering. Essentially, direct filtering of kinetic equations would allow us to consider good schemes, developed in statistical physics, in order to obtain closure approximations for nonlinear evolution equations.

Even though only the first steps have been done for deriving turbulence models from kinetic theory, this appears a very promising challenge for understanding rigorously the theoretical foundations of turbulence [101]. As discussed in Chapter 1, mesoscopic modeling exactly deals with the development of physical models where traditional statistical description of multi-particle systems is linked with usual macroscopic description of the phenomena. In the next Chapter 5, the pseudo-kinetic models will be discussed for achieving this goal.